Computing and understanding the CMB anisotropy

Nanna Bryne[1,2]

[1] Institute of Theoretical Astrophysics (ITA), University of Oslo, P.O. Box 1029 Blindern, N-0315 Oslo, Norway
[2] Center for Computing in Science Education (CCSE), Dept. of Physics, University of Oslo, P.O. Box 1048 Blindern, N-0316 Oslo, Norway
e-mail: `nanna.bryne@fys.uio.no`

May 27, 2023

ABSTRACT

Context. Project in the master-level subject AST5220 Cosmology II at the University of Oslo (UiO).
Aims. Write a self-contained program to compute theoretical CMB and matter power spectra, starting from fundamental principles.
Methods. By perturbing the background and considering the recombination history, we obtained the necessary quantities for calculating the CMB and matter power spectra. To get there, we used the Boltzmann and Einstein equations and linear perturbation theory, amongst other things. We condidered the conformal Newtonian gauge, and we neglected effects from neutrinos, helium, reionisation and polarisation. We used numerical methods s.a. Runge-Kutta and the trapezoidal rule for integrating.
Results. Our code provided satisfactory results to the point where neglegcted ingredients s.a. neutrinos were bound to play a role. All results prior to the power spectra essentially substantiate the physics we drew from the latter.
Conclusions. We succeded in building a code for our simple ΛCDM model with results that can be used to understand the governing physics at large and intermediate scales. However, small-scale physics can be understood better by relatively simple generalisations and improvents to the code.

Key words. cosmic microwave background – large-scale structure of universe

Contents

1. Introduction

The overall purpose of this project is to produce a program that calculates the Cosmic Microwave Background (CMB) power spectrum and predict the CMB and matter fluctuations through

it. We want to achieve this starting from first principles. A large part of this paper follows Callin (2006).

We consider the concordance model of cosmology model that a Euclidean universe currently dominated by non-baryonic cold dark matter (CDM) and a cosmological constant (Λ), namely the (flat) ΛCDM model. The cosmological constant Λ is used as a moniker for dark energy (DE). (Dodelson & Schmidt 2021)

There are in principle six free parameters to our ΛCDM universe, excluding the averages CMB temperature T_{CMB0}. The homogenous background is determined by the density parameter of the baryonic matter Ω_{b0}, the CDM Ω_{c0} and curvature Ω_{K0}, in addition to the Hubble constant $H_0 = 100h$ km s^{-1} Mpc^{-1}. To obtain power spectra, we need to include the primordial power spectrum defined by its amplitude $\mathcal{A}_{\text{s}}$ and spectral index n_{s}.

The structure of this paper reflects the project flow which was divided into four parts: the setup of the (unperturbed) background geometry in Sect. 2, studying the recombination history in Sect. 3, perturbing said background in Sect. 4 and finally calculating the CMB and matter power spectra in Sect. 5. Each section is equipped with its own short introduction, theoretical background, coding details, results and discussion.

Complementary material to this paper can be found in our Github repository at `https://github.com/nannabryne/AST5220`.

2. Background cosmology

The first ingredient in the aforementioned program is a numerical framework describing the (unperturbed) background geometry. Said geometry is determined by the Friedmann-Robertson-Walker (FRW) metric and, as a starting point, a flatness assumption. However, we keep the variables associated with the curvature, the reasoning behind which will become clear shortly.

We want to describe the evolution of the Hubble parameter, conformal time and distance measures, all as functions of the logarithmic scale factor, $x = \ln a$, working as the main time variable in this paper. This is to be done with the use of the fiducial parameters ("fiducials") from Planck Collaboration et al. (2021).

The implementation of these functions results in a cosmological model that we can play around with. Our next task is to use observational data from Betoule et al. (2014) to tweak the default cosmological parameters and evaluate their credibility, curvature being one of the parameters. In particular, we will use a Monte Carlo Markov Chain (MCMC) with Metropolis algorithm to explore the parameter space of our model to infer their properties and compare them with observations from supernovae.

MCMC is a popular statistical technique used in various fields besides cosmology. The Metropolis algorithm, a simple and widely used MCMC method, generates a Markov chain of samples in a data set that converge to the target distribution by iteratively accepting or rejecting proposed moves in parameter space based on a set of acceptance criteria.

2.1. Theory

The FRW line element in flat space is given by

$$ds^2 = -c^2\,dt^2 + a^2(t)\delta_{ij}\,dx^i\,dx^j \quad | \; d\eta \equiv c\,dt\,a^{-1}(t)$$
$$= a^2(t)\left(-d\eta^2 + \delta_{ij}\,dx^i\,dx^j\right). \tag{1}$$

Before we proceed, we substitute $a \to e^x$ (recall: $x = \ln a$). The cosmic time t and Hubble parameter H ($= dx/dt$) will be replaced by the conformal time η ($d\eta = c e^{-x}\,dt$) and conformal

Hubble parameter $\mathcal{H} \equiv aH$ ($= c\,dx/d\eta$). We write the Friedmann equations in terms of our preferred variables, which for the first one becomes

$$\mathcal{H}(x) = H_0\sqrt{\Omega_{\text{m0}}e^{-x} + \Omega_{\text{r0}}e^{-2x} + \Omega_{\text{K0}} + \Omega_{\Lambda 0}e^{2x}}, \tag{2}$$

the components of which are to be discussed shortly. The operator

$$\frac{d}{dx} = \frac{c}{\mathcal{H}}\frac{d}{d\eta} = \frac{1}{H}\frac{d}{dt} \tag{3}$$

proves useful, giving both the ordinary differential equation (ODE) for $\eta(x)$ and $t(x)$,

$$\frac{d\eta}{dx} = \frac{c}{\mathcal{H}(x)}\,; \qquad\qquad \eta(x_{\text{init}}) = \eta_{\text{init}}, \tag{4a}$$

$$\frac{dt}{dx} = \frac{1}{H} = \frac{e^x}{\mathcal{H}(x)}\,; \qquad\qquad t(x_{\text{init}}) = t_{\text{init}}, \tag{4b}$$

where, in theory, $x_{\text{init}} \to -\infty$ and the initial conditions $t_{\text{init}}, \eta_{\text{init}} \to 0$. However, we can solve Eq. (4) analytically in the very early universe and in Sect. 2.1.2 we present these expressions (Eq. (13)).

The conformal time is a useful time measure for large-scale cosmology as it takes into account the expansion of the universe. $\eta(x)$ measures the comoving distance that non-interacting photons could have travelled since the beginning where $x = -\infty$ ($t = 0$). Thus, the conformal time represents an upper limit to how far information could possibly travel. We say that regions that are separated by distances larger than this quantity are causally *dis*connected. For this reason, some books refer to $\eta(x)$ as the comoving horizon. (Dodelson & Schmidt 2021)

Finally, the cosmological redshift $z = e^{-x} - 1$ will be used as an auxiliary time variable.

2.1.1. Density parameters

We assume the constituents of the universe to be cold dark matter (CDM (c)), baryons (b), photons (γ), neutrinos (ν) and a cosmological constant (Λ). We may regard the curvature (K) as a constituent as well. The evolution of the density parameter Ω_s associated with cosmological component $s \in \{c, b, \gamma, \nu, \Lambda, K\}$ can be described in terms of our preferred variables as

$$\Omega_s(x) = \frac{\Omega_{s0}}{e^{(1+3w_s)x}\mathcal{H}^2(x)/H_0^2}\,; \quad \Omega_{s0} \equiv \Omega_s(x = x_0), \tag{5}$$

where H_0 is the Hubble constant, $x_0 = \ln a_0 = 0$ means *today* and the *equation of state* parameter w_s is a constant intrinsic to the species s. As a notational relief, we introduce the parameters associated with total matter (m) and relativistic particles (r) such that $w_{\text{m}} = 0$, $w_{\text{r}} = 1/3$, $w_\Lambda = -1$ and $w_{\text{K}} = -1/3$, and

$$\Omega_{\text{m}} = \Omega_{\text{c}} + \Omega_{\text{b}} \quad \text{and} \quad \Omega_{\text{r}} = \Omega_\gamma + \Omega_\nu. \tag{6}$$

Eq. (5) requires the current values of the density parameters. The observed CMB temperature today T_{CMB0} gives today's photon density

$$\Omega_{\gamma 0} = 2\frac{\pi^2}{30}\frac{(k_{\text{B}}T_{\text{CMB0}})^4}{\hbar^3 c^5}\frac{8\pi G}{3H_0^2}, \tag{7}$$

and followingly the neutrino density today

$$\Omega_{\nu 0} = N_{\text{eff}} \cdot \frac{7}{8}\left(\frac{4}{11}\right)^{4/3}\Omega_{\gamma 0}, \tag{8}$$

N_{eff} being the effective number of massless neutrinos. From the Friedmann equations, the total density adds up to one, so we can determine the cosmological constant through $\Omega_{\Lambda 0} = 1 - \sum_s \Omega_{s0}$. Together with current values for the remaining densities, we have the evolution of all the considered constituents' densities as functions of x. This allows us to pinpoint the time when the total matter and radiation densities are equal—the "radiation-matter equality"—as $\Omega_{\text{m}}(x = x_{\text{eq}}) = \Omega_{\text{r}}(x = x_{\text{eq}})$. Further, we find the time at which the universe becomes dominated by the cosmological constant as $\Omega_{\Lambda}(x = x_{\Lambda}) = \Omega_{\text{m}}(x = x_{\Lambda})$. We obtain the analytical expressions

$$x_{\text{eq}} = \ln \frac{\Omega_{\text{r}0}}{\Omega_{\text{m}0}} \quad \text{and} \quad x_{\Lambda} = \frac{1}{3} \ln \frac{\Omega_{\text{m}0}}{\Omega_{\Lambda 0}}. \tag{9}$$

2.1.2. Cosmic expansion

To study the geometry of the universe, we want to know when the expansion started, i.e. when the universe started accelerating: $\mathrm{d}^2 a / \mathrm{d}t^2$. It is trivial to show that this condition is equivalent to requiring $\mathrm{d}\mathcal{H}/\mathrm{d}x \,|_{x=x_{\text{acc}}} = 0$. In appendix A we present analytical expressions for the derivatives of $\mathcal{H}(x)$ in x. Studying these expressions, we expect to see that the start of acceleration and time of matter-dark energy transition are close to each other ($x_{\text{acc}} \sim x_{\Lambda}$). Using Eq. (A.3) and arguing that the radiation term vanishes, we get

$$x_{\text{acc}} = \frac{1}{3} \ln \frac{\Omega_{\text{m}0}}{2\Omega_{\Lambda 0}} = x_{\Lambda} - \frac{1}{3} \ln 2 \tag{10}$$

for the acceleration onset.

The first Friedmann equation can be written in the general form

$$\mathcal{H}(x) = H_0 \sqrt{\sum_s \Omega_{s0} \mathrm{e}^{-(1+3w_s)x}}, \tag{11}$$

where sum over s is a sum over the constituents in the universe ($s \in \{\text{m}, \text{r}, \Lambda, \text{K}\}$). In an era where e.g. radiation dominates heavily ($\Omega_{\text{r}}(x) \to 1$), the parameter resembles that of a universe with $\Omega_{\text{r}0} = 1$ and so $\mathcal{H}(x) \simeq H_0 \sqrt{\Omega_{\text{r}0} \mathrm{e}^{-2x}}$. In more general terms, the conformal Hubble factor during an era dominated by a collection of particles with the same equation of state—a species s—is approximated

$$\mathcal{H}(x) \simeq H_0 \sqrt{\Omega_{s0}} \mathrm{e}^{-\frac{x}{2}(1+3w_s)}. \tag{12}$$

If for said species we have $\Omega_s(x) \simeq 1$, we get $\Omega_{s'}(x) \ll 1$ for the others, and we expect this to be very close to equality.

In the very early universe, only relativistic particles were present. Conveniently, this gives nice expressions for the initial conditions for Eq. (4):

$$\eta_{\text{init}} = \int_{-\infty}^{x_{\text{init}}} \mathrm{d}x \, \frac{c\mathrm{e}^x}{H_0 \sqrt{\Omega_{\text{r}0}}} = \frac{c}{\mathcal{H}(x_{\text{init}})} \tag{13a}$$

$$t_{\text{init}} = \int_{-\infty}^{x_{\text{init}}} \mathrm{d}x \, \frac{\mathrm{e}^x \mathrm{e}^x}{H_0 \sqrt{\Omega_{\text{r}0}}} = \frac{\mathrm{e}^{x_{\text{init}}}}{2\mathcal{H}(x_{\text{init}})} \tag{13b}$$

Choosing such initial conditions, it is important to make sure $x_{\text{init}} \ll x_{\text{eq}}$ so that the approximation $\mathcal{H}(x) \simeq H_0 \sqrt{\Omega_{\text{r}0}} \mathrm{e}^{-x}$ is viable.

2.1.3. Distance measures

Say we want to allow for the possibility of an open ($\kappa < 0$) or closed ($\kappa > 0$) universe, as opposed to the initial flatness ($\kappa = 0$) assumption. In spherical coordinates, the FRW line element (Eq. (1)) is

$$ds^2 = \mathrm{e}^{2x} \left(-\mathrm{d}\eta^2 + \frac{\mathrm{d}r^2}{1 - \kappa r^2} + r^2 d\Omega^2 \right), \tag{14}$$

where $d\Omega^2 = \mathrm{d}\theta^2 + \sin^2\theta \, \mathrm{d}\phi^2$ and $\kappa \equiv -\Omega_{\text{K}0} H_0^2/c^2$. Consider a radial null curve, e.g. a radially moving ($\mathrm{d}r < 0$; $d\Omega^2 = 0$) photon ($ds^2 = 0$) travelling from a distance r at conformal time η to reach Earth ($r = 0$) today ($\eta = \eta_0$). Eq. (14) gives

$$\int_r^0 \mathrm{d}r' \, \frac{-1}{\sqrt{1 - \kappa r'^2}} = \int_\eta^{\eta_0} \mathrm{d}\eta' \tag{15}$$

of which the right-hand side (r.h.s.) is the comoving distance $\chi = \eta_0 - \eta$. We evaluate the left integral in Eq. (15) and find

$$r(\chi) = \begin{cases} \sin\left(\sqrt{|\kappa|}\chi\right)/\sqrt{|\kappa|} & \Omega_{\text{K}0} < 0 \\ \chi & \Omega_{\text{K}0} = 0 \\ \sinh\left(\sqrt{|\kappa|}\chi\right)/\sqrt{|\kappa|} & \Omega_{\text{K}0} > 0 \end{cases} . \tag{16}$$

The angular diameter distance of an object of physical size D and angular size θ is $d_A = D/\theta$. From Eq. (14) we get $\mathrm{d}D = r\mathrm{e}^x \, \mathrm{d}\theta$ and so

$$d_A(x) = r\mathrm{e}^x. \tag{17}$$

The luminosity distance is $d_L = d_A \mathrm{e}^{-2x}$, giving

$$d_L(x) = r\mathrm{e}^{-x}. \tag{18}$$

2.2. Implementation details

The code we wrote included a class in C++ representing the background. In particular, this class requires current values of the density parameters $\Omega_{\text{b}0}$, $\Omega_{\text{c}0}$ and $\Omega_{\text{K}0}$, the CMB temperature today ($T_{\text{CMB}0}$) and the effective neutrino number (N_{eff}). In addition, the class needs the "little" Hubble constant $h = H_0$ [100 km s^{-1} Mpc^{-1}]. The remaining density parameters are computed as elaborated in Sect. 2.1. Amongst the class methods are functions for computing $\mathcal{H}(x)$, $\mathrm{d}\mathcal{H}(x)/\mathrm{d}x$, $\mathrm{d}^2\mathcal{H}(x)/\mathrm{d}x^2$ and $\Omega_{s0}(x)$ for some x, as well as code that solves the ODEs for $\eta(x)$ and $t(x)$. Another vital method is the one that yields the luminosity distance $d_L(x)$ for some x.

The specifics of our model was found from fits from Planck Collaboration et al. (2021):

Hubble constant:	$h = 0.67$
CMB temperature:	$T_{\text{CMB}0} = 2.7255$ K
effective Neutrino number:	$N_{\text{eff}} = 3.046$
baryon density:	$\Omega_{\text{b}0} = 0.05$
CDM density:	$\Omega_{\text{c}0} = 0.267$
curvature density:	$\Omega_{\text{K}0} = 0$

$$\tag{19}$$

This gave the following derived parameters:

photon density:	$\Omega_{\gamma 0} = 5.51 \times 10^{-5}$
neutrino density:	$\Omega_{\nu 0} = 3.81 \times 10^{-5}$
DE density:	$\Omega_{\Lambda 0} = 0.683$

$$\tag{20}$$

We evaluated the various quantities over $x \in [-20, 5]$, the same interval for which we numerically solved the ODEs for $\eta(x)$ and $t(x)$ in Eq. (4), setting $x_{\text{init}} = -20$ in Eq. (13). For integration method, we used Runge-Kutta 4 (RK4). We used the ODE-solver from the GNU Scientific Library (GSL). Henceforth, we refer to the specifics of such a solver as "RK$N(\log_{10} h, \log_{10} \varepsilon, \log_{10} \tilde{\varepsilon})$" where N is the order of the RK algorithm, h the step size, and ε and $\tilde{\varepsilon}$ the absolute and relative error, respectively. The default solver will be RK4 := RK4$(-3, -7, -7)$.

After controlling our model by comparing numerical results to analytical expressions in limit cases, we turned our attention to the observational data from Betoule et al. (2014). The data set is constructed as follows: for each redshift z_i, there is an observed luminosity distance $d_L^{\text{obs}}(z_i)$ and an associated error $\sigma_{\text{err}}(z_i)$.

Subsequently, we wrote a script to perform an MCMC for the parameters h, Ω_{m0} and Ω_{K0}. Running said script, we compared the computed luminosity distance $d_L(z)$ from a cosmological model (an instance of the class) to the observed luminosity distance $d_L^{\text{obs}}(z)$ through the χ^2-function,

$$\chi^2(h, \Omega_{\text{m0}}, \Omega_{\text{K0}}) = \sum_{i=1}^{N} \frac{\left(d_L(z_i; h, \Omega_{\text{m0}}, \Omega_{\text{K0}}) - d_L^{\text{obs}}(z_i) \right)^2}{\sigma_{\text{err}}^2(z_i)}, \qquad (21)$$

where $N = 31$ is the number of data points. The best-fit model was considered as the one for which $\chi^2 = \chi_{\text{min}}^2$, the lowest number found by the algorithm. A good fit is considered to have $\chi^2/N \sim 1$.

The MCMC analysis was characterised by a maximum of 10 000 iterations and the following limitations:

$$
\begin{aligned}
0.5 \leq \quad & h \quad \leq 1.5 \\
0.0 \leq \quad & \Omega_{\text{m0}} \quad \leq 1.0 \\
-1.0 \leq \quad & \Omega_{\text{K0}} \quad \leq 1.0
\end{aligned}
\qquad (22)
$$

They were initialised by sample from a uniform distribution in the respective range. Once the code was executed successfully, we discard the first 200 samples, expecting this to be the approximate burn-in period for of the Metropolis MCMC.

2.3. Results

The familiar plot of the density parameters as functions of the logarithmic scale factor is presented in Fig. 1 together with markings of important milestones in the history of the universe (see Table 1).

The conformal Hubble factor and its derivatives are presented in Fig. 2 over-plotted with analytical predictions from the different eras (Table A.1). In the same figure you will find the product of the conformal time and Hubble factor.

The relationship between the cosmic and conformal time is demonstrated in Fig. 3, both quantities given in gigayears ("giga-annum" (Ga)).

We present the time of various milestones in the history of the universe, given this model, in Table 1 in our main time variable, redshift and cosmic time.

2.3.1. Supernova fitting

Before adjusting any parameters, we compared our initial model with the supernova data from Betoule et al. (2014). This by-eye comparison is found in Fig. 4. We demonstrated the model favoured by the data in the same plot.
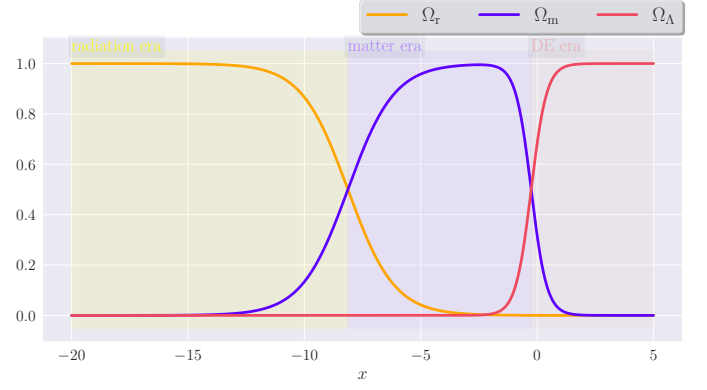
Fig. 1: The graphs show the evolution of the total matter density $\Omega_{\text{m}}(x)$, the total radiation density $\Omega_{\text{r}}(x)$ and the dark energy density $\Omega_\Lambda(x)$. The era of radiation ($x < x_{\text{eq}}$), matter ($x_{\text{eq}} < x < x_\Lambda$) and cosmological constant ($x > x_\Lambda$) domination are marked in yellow, purple and red, respectively.

Table 1: The values of the logarithmic scale factor x, the redshift z and the cosmic time t corresponding to four important milestones in the history of the universe.

	x	z	t
Rad.-matter equality	-8.132	3400	51.06 ka
Acceleration onset	-0.4869	0.6272	7.752 Ga
Matter-DE equality	-0.2558	0.2915	10.37 Ga
Today	-0.000	0.000	13.86 Ga
Conformal time today:			$\eta_0 = 46.32c$ Ga

The MCMC yielded $\chi_{\text{min}}^2 = 29.28$ for the best-fit. We present confidence regions for Ω_{m0} and $\Omega_{\Lambda 0}$ in Fig. 5a at two levels; 68.4% and 95.5%. The distribution of the curvature parameter is shown in Fig. 5b. As for the Hubble constant, the distribution is found in Fig. 5c. The distributions were fitted as normal distributions (demonstrated in Fig. 5) $\mathcal{N}(\mu, \sigma)$ with average μ (best-fit) and standard deviation σ (error). We got the following set of new best-fits:

$$
\begin{aligned}
h &= 0.70 \pm 0.01 \\
\Omega_{\text{m0}} &= 0.26 \pm 0.10 \\
\Omega_{\Lambda 0} &= 0.66 \pm 0.16 \\
\Omega_{\text{K0}} &= 0.08 \pm 0.25
\end{aligned}
\qquad (23)
$$

2.4. Discussion

The graphs in Fig. 1 show that prior to $x \sim -15$, radiation was the prevailing constituent of matter and energy density in the universe, making $x_{\text{init}} = -20$ in Sect. 2.1.2 a valid choice. The radiation era is followed by an era of matter domination before the universe enters its current epoch where dark energy is the preeminent contributor to the cosmic energy budget. The universe has not yet become overwhelmed by the dark energy, however, and we can see that we are currently in a transitional period between total matter domination and total DE domination. The graphs also show that this transitional period is much quicker than the previous one, and that just before matter-DE equality ($x = x_\Lambda$), the universe starts accelerating ($x = x_{\text{acc}}$). We clearly see the relation between the dark energy suddenly becoming significant and the universe accelerating.
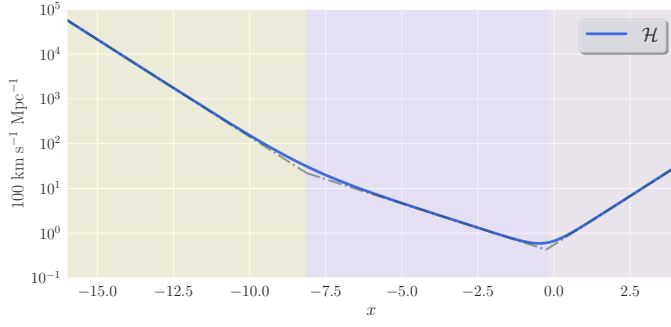
(a) The conformal Hubble factor $\mathcal{H}(x)$. The over-plotted dash-dotted line is the corresponding analytical estimate.
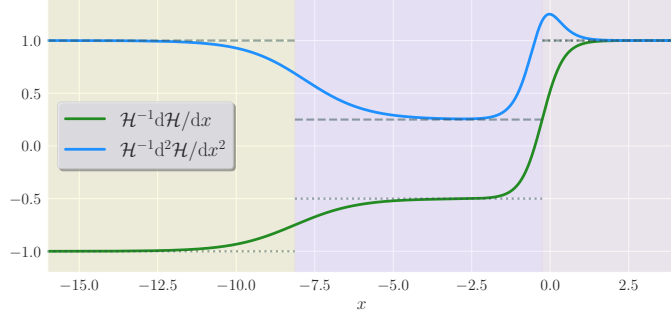
(b) The single and double derivative of the conformal Hubble factor, scaled with the factor itself, $\frac{1}{\mathcal{H}(x)}\frac{d\mathcal{H}(x)}{dx}$ and $\frac{1}{\mathcal{H}(x)}\frac{d^2\mathcal{H}(x)}{dx^2}$. The over-plotted dotted and dashed lines are the analytical estimates to the first and second derivative, respectively.
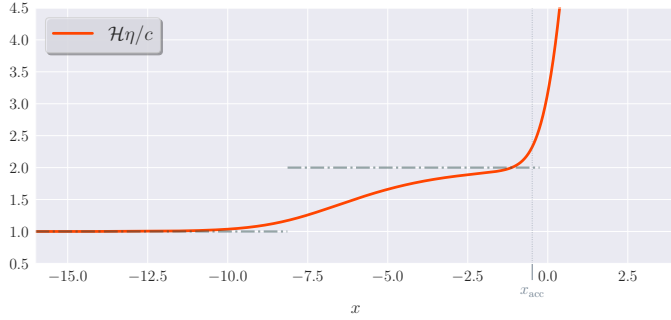

(c) The product of the conformal time and Hubble factor, divided by the speed of light, $\mathcal{H}(x)\frac{\eta(x)}{c}$. The solid graph blows up at late times. The over-plotted dash-dotted line is the corresponding analytical estimate (for single-substance universe).

Fig. 2: Plots demonstrating quantities related to the conformal Hubble parameter $\mathcal{H}(x)$ and the conformal time $\eta(x)$ as functions of logarithmic scale factor x. The dashed and/or dotted graphs are the predictions from Table A.1, i.e. what we expect in each era (indicated by different background colours, following Fig. 1) if all non-prevailing constituents can be neglected. The beginning of acceleration is indicated by a humble vertical line.

Our results, as shown in the graphs in Fig. 2, demonstrate that our code gives sensible results when modelling the evolution of the universe. The changes in the density parameters depicted in Fig. 1 offer insight into the transitional periods shown in Fig. 2a and Fig. 2b, which correspond to eras where no single substance dominates the universe. These findings are consistent with existing knowledge of the universe's history. Additionally, we observe that the conformal time cannot be accurately predicted in the same way for later eras, as demonstrated in Fig. 2c, exactly as expected (c.f. appendix A).

In this model, the redshift of 3400 marks the epoch of radiation-matter equality, while the universe entered its current epoch approximately 3.5 gigayears ago as shown in Table 1. Ad-
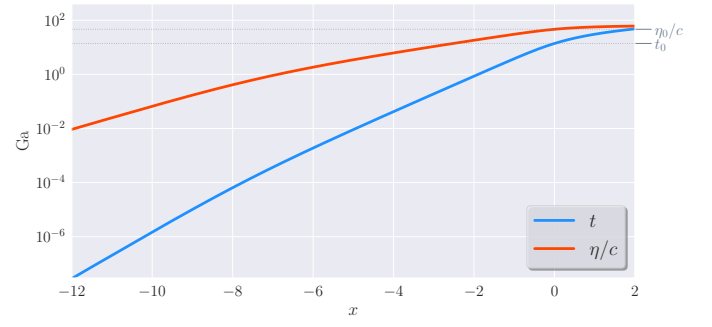
Fig. 3: Cosmic time $t(x)$ and conformal time per speed of light $\frac{\eta(x)}{c}$. Note the logarithmic y-axis.
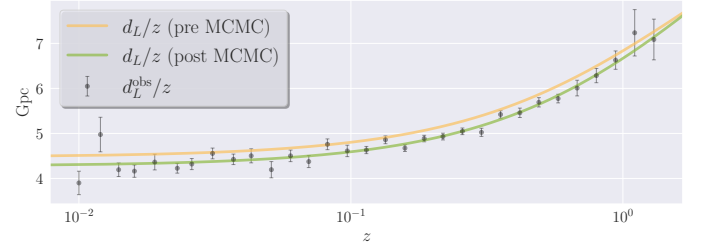
Fig. 4: The observed (dots) and computed (lines) luminosity distance per redshift $\frac{d_L^{\mathrm{obs}}(z) \pm \sigma_{\mathrm{err}}(z)}{z}$ and $\frac{d_L(z)}{z}$. The yellow line represents the fiducial model, whilst the green line is the revised model resulting from the MCMC.

ditionally, our analysis reveals that the universe is estimated to be 13.9 gigayears old and has been accelerating for almost half of that time, starting at the age of 7.8 gigayears. These predictions differ slightly from those reported in the literature, such as an age of $t_0 = 13.78$ in Dodelson & Schmidt (2021). It is sufficient to argue that the main reason for such deviations is the (small) difference in choice of cosmological parameters. However, we would like to address the computational limitations: the choice of grid for x may introduce numerical vulnerabilities that propagate into other variables. For instance, as illustrated in Fig. 3, over 10 gigayears can pass between $x = -2$ and $x = 0$, even though we started integrating from $x = x_{\mathrm{init}} = -20$.

2.4.1. Supernova fitting

The comparison of our model's luminosity distance with observational data, as shown in Fig. 4 (ignoring the posterior green graph), suggests that our model could benefit from some adjustments. While the deviations are not too far off, it is clear that there is some room for improvement. However, it is important to note that the discrepancies may not be solely due to the three parameters we chose to study.

To further constrain our model, we performed an MCMC analysis and examined the resulting distributions of parameters. The scatter plot in Fig. 5a shows that our model requires an accelerating universe ($d\mathcal{H}/dx\,|_{x=x_0} > 0$) with a strictly positive cosmological constant ($\Omega_{\Lambda 0} > 0$). We notice that the Planck parameters lie within the 1σ region for (Ω_{m0}, $\Omega_{\Lambda 0}$), along the flat line. This is not the case for all the parameters, however.

Interestingly, the data clearly prefer a slightly higher value for the little Hubble parameter h than our fiducial value of 0.67, as shown in the narrow histogram in Fig. 5c. The PDFs of the
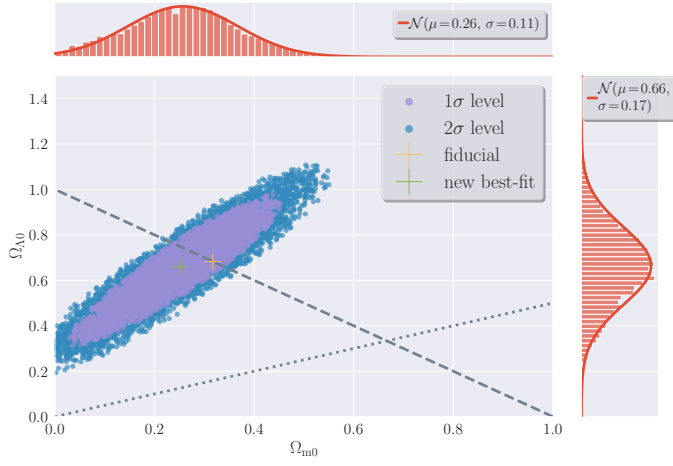
(a) The dots give constraints on the parameters that quantify the contribution of matter and cosmological constant to the cosmic energy budget today (Ω_{m0}, $\Omega_{\Lambda0}$). The Planck parameters from Eq. (19) and Eq. (20) and the new best-fit parameters are indicated by crosses. The dashed grey line points to a flat universe; below/above this meaning an open/closed universe. The dotted grey line signifies zero acceleration; below/above indicating a decelerating/accelerating universe. The distributions of the accepted samples of Ω_{m0} and $\Omega_{\Lambda0}$ are illustrated by the top and right panel, respectively.
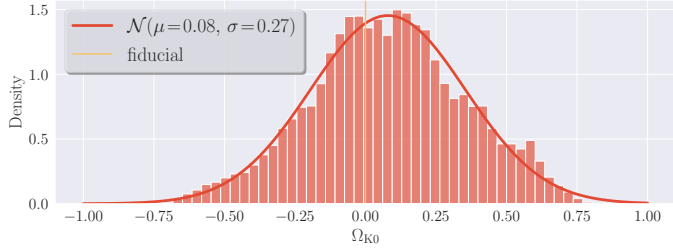
(b) Posterior distribution of parameter quantifying the contribution of curvature to the cosmic energy budget today.
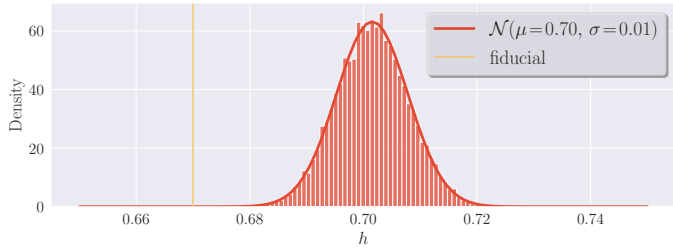
(c) Posterior distribution of the Hubble constant $h = H_0$ [100 km s^{-1} Mpc^{-1}].

Fig. 5: Results from the MCMC of 10 000 iterations. The histograms show the distributions of accepted samples and the curves are their PDFs.

density parameters Ω_{m0} and $\Omega_{\Lambda0}$ are much broader, but the algorithm manages to narrow the possibilities down significantly.

One potential concern is the uncertainty in the curvature parameter Ω_{K0}, as shown in Fig. 5. The data seem to favour a negatively curved universe, but the allowed range is quite broad. This may indicate that our model needs further refinement to better account for the effects of curvature.

Overall, our primitive MCMC analysis provides valuable insights into the constraints on the parameters of our model and highlights areas where further improvements could be made. Other than with observational data from supernovae, there are several ways of constraining the cosmological parameters, such as measuring the CMB anisotropies. Planck Collaboration et al. (2021) provides a set of cosmological parameters that are significantly more solid, in the sense that their results are tested and

compared thoroughly. This is why we proceed using the fiducials from Eq. (19) and Eq. (20).

3. Recombination history

After the Big Bang, the universe was in a state of high temperature and density, making it impossible for atoms to form. Instead, all matter existed as a highly ionised plasma. It was only when the universe began to expand and cool down that the conditions allowed for the combination of ions (protons) and electrons. This process resulted in the formation of atoms, primarily hydrogen and helium, during the "epoch of recombination" around 380 000 years after the Big Bang, when the temperature had dropped to around 3000 K. Prior to this, photons could not travel freely through the ionised plasma as they were scattered by free electrons. However, as free electrons combined with other baryons to form neutral atoms during recombination, the mean free path of the photons increased. The photons emitted during this period make up the CMB radiation.

We will in this section examine the free electron fraction and following the optical depth and visibility function. From these quantities, we find the time of recombination and surface of last scattering. In addition, we will compute the freeze-out free electron fraction and sound horizon at decoupling. Throughout this section, we ignore helium completely.

3.1. Theory

The process that is keeping the photons (γ) coupled to electrons (e^-) in the early universe is called Thomson scattering and is the low-energy case of Compton scattering,

$$\gamma + e^- \leftrightarrows \gamma + e^-, \tag{24}$$

and considered to be the major source of opacity in the early universe. Going forward in time, the universe expanded and therefore cooled down, eventually to the temperature for which the combination of electrons and protons (p)—the formation of neutral hydrogen atoms (H)—was energetically favourable. As a result, the amount of free electrons (and protons), compared to the total number of baryons in the universe, rapidly decreased. As direct recombinations to the ground state are highly unlikely, a hydrogen atom generally arises from an electron in a high energy state that immediately decays to its ground state, emitting a photon in the process;

$$e^- + p \leftrightarrows H + \gamma. \tag{25}$$

There are two main pathways from the first excited state ($n = 2$) to the ground state ($n = 1$):

– $2p \rightarrow 1s$: decay through the emission of a Lyman-α photon that is (almost exclusively) to be reabsorbed by another ground state hydrogen
– $2s \rightarrow 1s$: through the very slow procxess of 2-photon decay

These basic principles are amongst those that Jim Peebles and collaborators (see Peebles 1968) adopted in their model of non-equilibrium recombination history of hydrogen, described by the differential equation for the free electron abundance we call the *Peebles equation* (Eq. (33)). There are numerical difficulties when solving this equation for very early times—this is where we address the work of Meghnad Saha in 1920. The *Saha equation* (Eq. (29)) is applicable in systems of chemical equilibrium

and relates the number densities of reactants to those of the products in a reaction (assuming the equilibrium density of each element is known). At early times, this is a viable assumption, and we can examine the abundance of free electrons in the universe at all times. (Peebles 1968; Ma & Bertschinger 1995; Callin 2006)

The aforementioned equations originate from the Boltzmann equation, which can take the general form

$$\frac{1}{n_1 e^{3x}} \frac{d\left(n_1 e^{3x}\right)}{dx} = -\frac{\Gamma_1}{\mathcal{H}(x) e^{-x}} \left[1 - \frac{n_3 n_4}{n_1 n_2} \frac{n_1^{(0)} n_2^{(0)}}{n_3^{(0)} n_4^{(0)}}\right] \qquad (26)$$

for a reaction $(1) + (2) \leftrightarrows (3) + (4)$, where n_j $(n_j^{(0)})$ denotes the (equilibrium) number density of $j = 1, 2, 3, 4$. The interaction rate $\Gamma_1 = n_2 \langle \sigma v \rangle$ depends on the thermally averaged cross-section $\langle \sigma v \rangle$ that we get from quantum field theory (QFT). We provide a qualitative discussion of this equation below.

If $\Gamma_1 \gg \mathcal{H} e^{-x}$ (recall: $\mathcal{H}(x) e^{-x} = H$, the expansion rate of the universe), the rate at which the interaction is happening is large enough to keep up with the expansion of the surroundings, and the system is driven towards equilibrium ($n_j = n_j^{(0)}$). When the interactions are sufficiently efficient, we will have equilibrium and the bracket in Eq. (26) goes to zero. This is how the Saha equation arises. One may wonder why we consider this approximation at all when we have a completely fine ODE. However, in numerical analysis, the subtraction in said bracket may result in a "catastrophic cancellation", hence the Saha approximation for the equilibrium case is necessary.

Once $\Gamma_1 \sim \mathcal{H} e^{-x}$, the interaction rate is comparable to the expansion rate and this dynamic equilibrium is no longer upheld. We say that the particles involved *decouple* from the primordial plasma. After decoupling, a species evolves independently.

When $\Gamma_1 \ll \mathcal{H} e^{-x}$, the interaction is irrelevant and the r.h.s. of Eq. (26) is practically zero and n_1 goes as e^{-3x}, meaning that the number density of (1) is constant in a comoving volume. If (1) is massive, we say that it *freezes out* at this point, and expect to find the same fractional abundance today. That is, of course, when ignoring the epoch of reionisation, which would complicate the evolution of the quantities in this section quite severely.

3.1.1. Optical depth and visibility

Photons travelling through a medium may be absorbed. The intensity of light emitted from a distance x is reduced by the factor $e^{-\tau(x)}$ where $\tau(x)$ is the optical depth of the medium. An optically thin ($\tau \ll 1$) medium does little or no absorbing, whereas an optically thick ($\tau \gg 1$) substance does not let much, if any, light pass through. In cosmology, Thomson scattering is predominantly responsible for the absorption of photons universe. This gives us the ODE for $\tau(x)$,

$$\frac{d\tau}{dx} = -\frac{c n_e \sigma_T e^x}{\mathcal{H}(x)}, \qquad (27)$$

with $\tau(0) = 0$ by definition, where σ_T is the Thomson scattering cross-section and n_e the electron density. A related quantity is the visibility function

$$\tilde{g}(x) = -e^{-\tau(x)} \frac{d\tau(x)}{dx}, \qquad (28)$$

a proper probability distribution obeying $\int_{-\infty}^{0} dx\, \tilde{g}(x) = 1$. The probability it describes, is that of a CMB photon's last interaction with an electron to have happened at x. This function will have a peak at the point in time when the mean free path

of the photons increased tremendously—at the last scattering surface—which happened immediately after the number of free electrons dropped dramatically. In mathematical terms, this decoupling happened when $\tilde{g}(x_*) = \max \tilde{g}(x)$.

We will take x_* to mean the logarithmic cosmic scale factor at the epoch of recombination, and our primary definition of this will be the peak of the visibility function. However, there are ambiguities to the definition of this point in time. For instance, the surface of last scattering can also be taken as the time when the universe is neither opaque nor transparent, i.e. the solution of $\tau(x = x_*) = 1$. As mentioned above, photons decoupled when the interaction rate of the photons was equal the expansion rate of the universe.

3.1.2. Hydrogen recombination

Before we can compute the optical depth, we need to know the electron number density, n_e, at all times. We define the free electron fraction $X_e \equiv n_e / n_b$ where n_b is the total baryon number density. Before recombination, that is for $x \ll x_*$, all hydrogen is completely ionised, meaning that $X_e(x \ll x_*) \simeq 1$. We will consider the 90% drop in fractional electron abundance mark the onset of recombination, i.e. when $X_e(x = x_*) = 0.1$. One should keep in mind that the number 0.1 is arbitrary and that this definition vary in the literature.

Consider the interaction that keeps electrons and protons in equilibrium with photons, i.e. Eq. (25). Letting n_s $(n_s^{(0)})$ denote the number density of a species/element s (in equilibrium), the corresponding equilibrium equation is

$$\frac{n_e n_p}{n_H} = \frac{n_e^{(0)} n_p^{(0)}}{n_H^{(0)}}, \qquad (29)$$

known as the *Saha equation*. Likewise, letting m_s refer to the mass of s, we can take the number density of neutral hydrogen to be

$$n_H = (1 - Y_P) n_b \simeq (1 - Y_P) \frac{\Omega_{b0} \rho_{cr0}}{m_H e^{3x}}; \quad \rho_{cr0} = \frac{3 H_0^2}{8\pi G}, \qquad (30)$$

where Y_P denotes the primordial helium mass fraction. We neglect helium s.t. $Y_P = 0$ and assume that all baryons are protons. Further, recognising the neutrality of the universe ensures $n_p = n_e$. Now, $n_b = n_p + n_H$ and

$$X_e = \frac{n_e}{n_e + n_H} = \frac{n_p}{n_p + n_H}. \qquad (31)$$

The evolution of the baryon temperature $T_b = T_b(x)$ is non-trivial, and the precision gained from implementing the exact model is dissapointing. It suffices to assume $T_b \approx T_\gamma = T_{CMB0} e^{-x}$. (Callin 2006)

Let $\Upsilon = \Upsilon(T_b) \equiv \epsilon_0 / (k_B T_b)$, where $\epsilon_0 \simeq 13.6$ eV is the binding energy of hydrogen, for notational ease. Multiplying Eq. (29) by n_b^{-1} and inserting expressions for $n_s^{(0)}$, we obtain the more suggestive form of the Saha equation

$$\frac{X_e^2}{1 - X_e} = \frac{1}{n_b} \left(\frac{m_e k_B T_b}{2\pi \hbar^2}\right)^{3/2} e^{-\Upsilon}; \quad X_e \lesssim 1. \qquad (32)$$

The constraints on X_e are that it is a positive number that cannot exceed 1 and the observation that it has to be close to 1. The latter constraint is due to the equilibrium assumption from which the Saha equation is derived: as X_e falls the reaction rate

for Eq. (25) falls and equilibrium is not guaranteed. To proceed, we need to solve the Boltzmann equation. More precisely, Jim Peebles needed to solve the Boltzmann equation, whereas we shall study the product; a first-order named ODE the *Peebles equation*. Said equation reads

$$\frac{\mathrm{d}X_e}{\mathrm{d}x} = \frac{C_r(T_{\mathrm{b}})}{\mathcal{H}(x)\mathrm{e}^{-x}} \left[\beta(T_{\mathrm{b}}) (1 - X_e) - n_{\mathrm{H}} \alpha^{(2)}(T_{\mathrm{b}}) X_e^2 \right], \tag{33}$$

where the necessary mathematical expressions are the following:

$$C_r(T_{\mathrm{b}}) = \frac{\Lambda_{2\gamma} + \Lambda_{\alpha}}{\Lambda_{2\gamma} + \Lambda_{\alpha} + \beta^{(2)}(T_{\mathrm{b}})} \tag{34a}$$

$$\Lambda_{2\gamma} = 8.227 \ \mathrm{s}^{-1} \tag{34b}$$

$$\Lambda_{\alpha} = \frac{\mathcal{H}\mathrm{e}^{-x}}{(8\pi)^2 n_{1s}} \left(\frac{3\epsilon_0}{\hbar c} \right)^3 \tag{34c}$$

$$n_{1s} \approx (1 - X_e) n_{\mathrm{H}} \tag{34d}$$

$$\beta^{(2)}(T_{\mathrm{b}}) = \beta(T_{\mathrm{b}}) \mathrm{e}^{3/4 \Upsilon} \tag{34e}$$

$$\beta(T_{\mathrm{b}}) = \alpha^{(2)}(T_{\mathrm{b}}) \left(\frac{m_e k_{\mathrm{B}} T_{\mathrm{b}}}{2\pi\hbar^2} \right)^{3/2} \mathrm{e}^{-\Upsilon} \tag{34f}$$

$$\alpha^{(2)}(T_{\mathrm{b}}) = \frac{8c\sigma_{\mathrm{T}}}{\sqrt{3\pi}} \sqrt{\Upsilon} \phi_2(T_{\mathrm{b}}) \tag{34g}$$

$$\phi_2(T_{\mathrm{b}}) \approx 0.448 \ln \Upsilon \tag{34h}$$

A detailed description of Eq. (34) is found in Peebles (1968). We provide a brief summary of the model.

The decay rates Λ_{α} and $\Lambda_{2\gamma}$ are the rates of the processes $2p \rightarrow 1s$ and $2s \rightarrow 1s$ mentioned in the beginning of Sect. 3.1, respectively. $\beta^{(2)}$ represents the Lyman alpha production. Thus, the correction factor C_r is the ratio between the net decay rate and the combined decay and ionisation rates from the first excited level. In other terms, C_r is the probability that a hydrogen atom in $n = 2$ actually reaches $n = 1$ through emission of a Lyman-α photon or two photons. The approximation of the number density of H in the ground state n_{1s} is sensible for $T_{\mathrm{b}} \ll 10^5$ K, i.e. for $x \ll \ln T_{\mathrm{CMB0}} - 5 \ln 10 \approx -10$. Finally, β is the ionization rate and $\alpha^{(2)}$ the recombination rate, where ϕ_2 is also a good approximation at low temperatures. (Dodelson & Schmidt 2021; Ma & Bertschinger 1995; Peebles 1968)

3.1.3. Sound horizon

The distance that a sound wave could propagate in the primordial plasma before photons decoupled is called "the sound horizon at decoupling", a quantity whose significance will become prominent in sections to come. We define the sound speed of a photon-baryon plasma as

$$c_s \equiv c \sqrt{\frac{1}{3(1 + R)}}, \tag{35}$$

where the baryon-to-photon energy ratio is defined as

$$R \equiv \frac{3\Omega_{\mathrm{b}}(x)}{4\Omega_{\gamma}(x)} = \frac{3\Omega_{\mathrm{b0}}}{4\Omega_{\gamma 0}} \mathrm{e}^x. \tag{36}$$

The comoving distance travelled by a sound wave—the sound horizon—at time x as the solution $s(x)$ to the ODE

$$\frac{\mathrm{d}s}{\mathrm{d}x} = \frac{c_s}{\mathcal{H}(x)}; \quad s(x_{\mathrm{init}}) = \frac{c_s(x_{\mathrm{init}})}{\mathcal{H}(x_{\mathrm{init}})}. \tag{37}$$

Evaluating $s_* \equiv s(x = x_*)$ gives the sound horizon at decoupling. At this point, the plasma through which sound waves propagate is no longer present and the waves are frozen in.

3.2. Implementation details

We implemented a class in C++ that assumes a background, an object of the class from Sect. 2.2, and a primordial helium abundance Y_P. The code we wrote calculated $X_e(x)$ (and $n_e(x)$) from the Saha and Peebles equations and computed $\tau(x)$ as well as $\tilde{g}(x)$, $\mathrm{d}\tilde{g}(x)/\mathrm{d}x$ and $\mathrm{d}^2\tilde{g}(x)/\mathrm{d}x^2$ for a given array of x-values. We added a computation of $s(x)$ to find the sound horizon at decoupling.

We ran an additional simulation where we assumed equilibrium all the way, that is we solved for $X_e(x)$ using only the Saha equation.

Electron fraction and number density The computation of $X_e(x)$ was divided into two parts. We let $X_e(x) > 0.99$ signify the Saha regime for which we use the Saha approximation in Eq. (32). Numerically speaking, the solution to this equation,

$$X_e(x) = \frac{\mathfrak{U}}{2} \left(-1 + \sqrt{1 + 4\mathfrak{U}^{-1}} \right); \quad \mathfrak{U} = \frac{1}{n_{\mathrm{b}}} \left(\frac{m_e k_{\mathrm{B}} T_{\mathrm{b}}}{2\pi\hbar^2} \right)^{3/2} \mathrm{e}^{\Upsilon}, \tag{38}$$

blows up for large values of $\mathfrak{U}$. Analytically we have $X_e \rightarrow 1$ as $\mathfrak{U} \rightarrow \infty$, so we circumvented the issue by letting $X_e = 1 \ \forall \ \mathfrak{U} > 10^7$. Outside the Saha regime, we used the last value of $X_e(x)$ (≈ 0.99) as initial condition on the Peebles ODE (Eq. (33)) and solved this for the remaining values of x. Here as well, we needed to address numerical stability concerns. Specifically, $\beta^{(2)}$ in Eq. (34e) was set to zero when the exponent was too large; $\Upsilon > 200$, i.e. at later times when $T_{\mathrm{b}} < 0.005\epsilon_0/k_{\mathrm{B}} \sim 800$ K.

The numerical integration was performed using RK4.

Optical depth and visibility We computed $\tau(x)$ by solving the simple ODE in Eq. (27) starting from $x = 0$ where $\tau(0) = 0$ and integrating backwards in time, using RK4.

We used the analytical expressions in Eq. (27) and Eq. (28) for $\mathrm{d}\tau(x)/\mathrm{d}x$ and $\tilde{g}(x)$, respectively, and found $\mathrm{d}^2\tau(x)/\mathrm{d}x^2$, $\mathrm{d}\tilde{g}(x)/\mathrm{d}x$ and $\mathrm{d}^2\tilde{g}(x)/\mathrm{d}x^2$ numerically.

Sound horizon The computation of $s(x)$ was a straight-forward numerical integration of Eq. (37) for $x \in [x_{\mathrm{init}}, 0]$, again using RK4. Having $x_{\mathrm{init}} = -20$ ensures radiation domination (see Fig. 1), so the initial condition is valid.

3.3. Results

The free electron fraction as computed from the Saha and Peebles equations in their respective regimes is plotted in Fig. 6. We added the result from using only the Saha equation. As elaborated in Sect. 3.2 we calculated the optical depth and visibility function and their derivatives. We present the optical depth and its derivatives in Fig. 7. The visibility function is demonstrated in Fig. 8, where we have included its derivatives scaled to be comparable to the original function.

Using the definitions of the time of last scattering surface and recombination presented in Sect. 3.1.1 and Sect. 3.1.2, we measured the logarithmic scale factor, redshift and cosmic time at these events. We present the results in Table 2 in addition to today's value of the freeze-out electron abundance and the sound horizon at decoupling. The number of significant figures is exaggerated to point out the small differences. The corresponding values resulting from the Saha equation is included in parentheses.
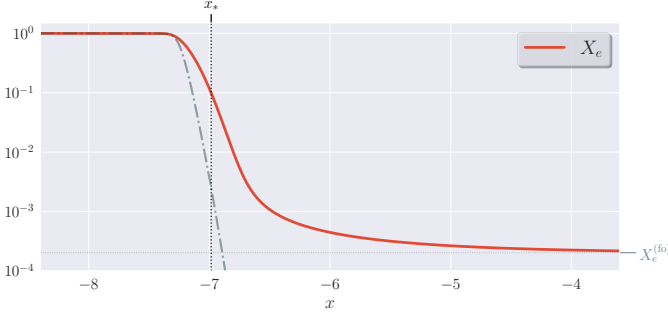
**Fig. 6:** The free electron fraction $X_e(x)$ resulting from the Saha and Peebles equations. The dash-dotted line represents the solution from the Saha equation only. Recombination onset is shown as the black, dotted vertical line. The freeze-out abundance $X_e^{(fo)} = X_e(0)$ is demonstrated as a dotted horizontal line.
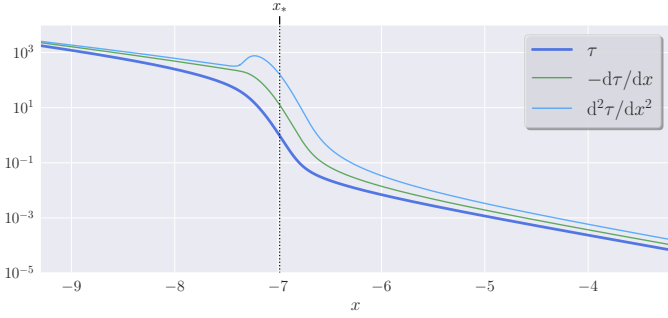
Fig. 7: The optical depth $\tau(x)$ and its derivatives $-\frac{d\tau(x)}{dx}$ and $\frac{d^2\tau(x)}{dx^2}$ as functions of logarithmic scale factor x. Recombination onset is shown as the dotted vertical line.
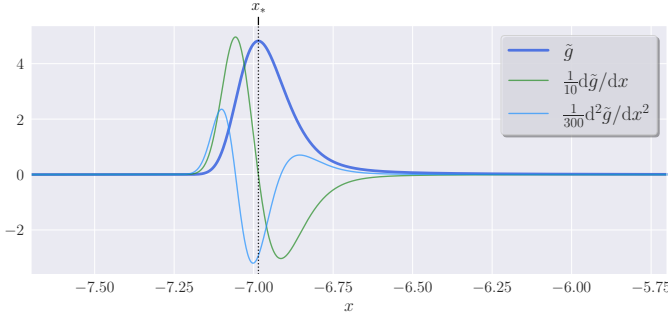
Fig. 8: The visibility function $\tilde{g}(x)$ and the shape of its derivatives $\frac{d\tilde{g}(x)}{dx}$ and $\frac{d^2\tilde{g}(x)}{dx^2}$ as functions of logarithmic scale factor x. Recombination onset is shown as the dotted vertical line.

In the analysis, we used that $x_* = -6.9853$ at the peak of the visibility function.

3.4. Discussion

Overall, the results presented in the figures in Sect. 3.3 resemble those of a corresponding analysis by Callin (see 2006, Fig. 1, 2).

The graphs in Fig. 6 demonstrate the invalidity of the Saha solution for later times. The solid graph indicates a freeze-out electron fraction of order $10^{-4} - 10^{-3}$, which we confirm in Table 2. We notice the decelerating decay rate at $x \sim -6.8$. Using our definitions of recombination onset and surface of last scatter-

Table 2: The values of the logarithmic scale factor x, the redshift z and the cosmic time t corresponding to two events in the history of the universe. Values in parentheses are those we get with only the Saha equation.

	x	z	t
Recombination onset			
$X_e = 0.1$	-6.9854	1079.8	377.95 ka
	(-7.1404)	(1260.9)	$(290.89$ ka$)$
Photon decoupling			
$\tilde{g} = \max \tilde{g}$	-6.9853	1079.7	378.04 ka
	(-7.1548)	(1279.3)	$(283.81$ ka$)$
$\tau = 1$	-6.9878	1082.3	376.50 ka
	(-7.1581)	(1283.5)	$(282.24$ ka$)$

Freeze-out free electron abundance:	$X_e^{(fo)} = 2.0261 \times 10^{-4}$
Sound horizon at decoupling:	$s_* = 145.30$ Mpc

ing, the Saha equation does not suffice for pinpointing the time for when these events occur. In this case, according to Table 2, the order of these events are reversed. However, these numbers rely on how we define the distinct events.

The optical depth in Fig. 7 tells us that the universe was very opaque before recombination, and that during the short period around recombination, the optical depth went from $\tau(-7.5) \sim 100$ to $\tau(-6.5) \sim 0.01$. After this epoch, the optical depth resumes its exponential decay. We see that $\tau(x_*) \approx 1$, as expected.

The visibility function is completely flat (zero) until just before $x = x_*$ where it rapidly increases to its maximum before an almost equally rapid decrease. However, there is a notable asymmetry in the probability function. The tail on the right side of the peak is longer than the one of the left. Together with Fig. 6, we take this to mean that, some time after recombination (see the slope in $X_e(x)$ at $x \sim -6.8$), there are still a significant portion of free electrons left to prevent photons to travel freely. In any case, the CMB photons last interacted with electrons between $x = -7.2$ and $x = -6$, most likely before $x = -6.7$.

Table 2 shows that recombination and photon decoupling occurred at redshift 1080 or 380 000 years after BB, consistent with concordance cosmology (e.g. Baumann (2015, Tab. 3.1)).[1] From this model, we get that the free electron abundance has ceased to be only a single free electron for every 5000 hydrogen atom, i.e. $X_e(x=0) = X_e^{(fo)} \approx 2 \times 10^{-4}$.

Sound waves managed to travel maximum 145 Mpc before frozen in. This length scale is imprinted in the CMB.

4. Growth of structure

In the previous sections, we have considered the homogeneous and isotropic universe. We now turn our attention to the *in*homogeneities in the matter and *an*isotropies in the cosmic distribution of photons—those which have given rise to the evolution of structure in the universe.

We will study perturbation quantities for small-scale physics, as well as for larger scales. From the photon temperature perturbations, we get the temperature source function which will be important when eventually computing the CMB spectrum. The following analysis is completely ignorant of neutrinos in the universe and photon polarisation.

---

[1] There is an implicit wiggle room when we say "consistent" in this context, as there are several ways of defining recombination onset and the last scattering surface.

In this section, we focus more on the mathematics and technicalities of the perturbations than on the physics driving them. The latter will be covered in more detail in Sect. 5.

4.1. Theory

The geometry of the spacetime is encoded in the Einstein tensor $G_{\mu\nu}$ that relates to the energy-momentum tensor $T_{\mu\nu}$ through the Einstein equation $G_{\mu\nu} = 8\pi G T_{\mu\nu}$. The latter quantity describes the distribution of energy and matter. The perturbed Einstein equation can be written

$$G_{\mu\nu}^{(0)} + \delta G_{\mu\nu} = 8\pi G \left(T_{\mu\nu}^{(0)} + \delta T_{\mu\nu} \right), \tag{39}$$

where we use (and will continue to use) superscript "(0)" to indicate the unperturbed quantity. Being primarily interested in the perturbations, it all boils down to using the Boltzmann equation solving and

$$\delta G_{\mu\nu} = 8\pi G \, \delta T_{\mu\nu} \tag{40}$$

in a clever way.[2] The metric is related to the Einstein tensor through $G_{\mu\nu} = \mathcal{R}_{\mu\nu} - \frac{1}{2} g_{\mu\nu} \mathcal{R}$, where $\mathcal{R}_{\mu\nu}$ and $\mathcal{R}$ is the Ricci tensor and scalar, respectively. Below is presented a short description of the quantities we aim to compute.

- Ψ and Φ are first-order spacetime corrections (potentials) to g^{00} and g^{ij}, respectively, both closely related to the Newtonian gravitational potential. We refer to Ψ as the gravitational potential and Φ as the spatial curvature.
- $\delta_{\rm c}$ and $\delta_{\rm b}$ are first-order density perturbations to non-relativistic matter, representing cold dark matter and baryonic matter, respectively.
- $u_{\rm c}$ and $u_{\rm b}$ are velocity perturbations to non-relativistic matter, representing cold dark matter and baryonic matter, respectively. They are *bulk* velocities in the longitudinal direction, and are themselves first-order terms.
- $\Theta_{\ell=0,1,\dots,\ell_{\max}}$ are the photon multipoles that show up when expanding the photon temperature fluctuations Θ into spherical harmonics. As we will see, the first two moments are related to the photon density perturbation to linear order δ_γ and the longitudinal photon velocity u_γ.

We will not go into detail in how to get from Eq. (40) to the set of equations we will eventually use, but rather keep in mind that the quantities $\delta_{\rm c,b}$, $u_{\rm c,b}$, Θ_ℓ, Φ and Ψ are deduced from the Einstein equation and first order linear perturbation theory. One should also keep in mind that the perturbation quantities are functions of time x *and* Fourier mode k (to be elaborated shortly), as this section will suffer from somewhat sloppy notation. In the following, we spare ourselves the eyesore that is the complete set of equations we will use and save this for appendix B.

Modes and scales Instead of real space of cosmic time t and physical position $\boldsymbol{x}$, we will work in the Fourier space ($\boldsymbol{x} \rightarrow \boldsymbol{k}$), so that all our quantities will generally be functions of Fourier mode $k = |\boldsymbol{k}|$ and our time variable $x = \ln a(t)$. That is, a function f of space and time is

$$f(t, \boldsymbol{x}) = \int \frac{d^3k}{(2\pi)^3} e^{i\boldsymbol{k}\cdot\boldsymbol{x}} f(x(t), \boldsymbol{k}), \tag{41}$$

and will notationally not be distinguished from its Fourier transform. Spatial derivatives of $f(t, \boldsymbol{x})$ become

$$\frac{\partial f(t, \boldsymbol{x})}{\partial x^i} \rightarrow i k_i f(x(t), \boldsymbol{k}). \tag{42}$$

The direction of the comoving wavevector $\boldsymbol{k}$ will be neglected or contained in other variables. We let $k = |\boldsymbol{k}|$ be the magnitude of a $\boldsymbol{k}$-mode. In summary:

$$f(t, \boldsymbol{x}) \rightarrow f(x, k)$$
$$\partial_i f(t, \boldsymbol{x}) \rightarrow i k f(x, k) \tag{43}$$

We use the Fourier modes k to classify the physical scales. The quantity k is a frequency, inverse proportional to a physical wavelength $\lambda_{\rm phys}$. This wavelength represents the spatial size of the causally connected region we consider when studying a k-mode. We separate roughly between three main regimes: those of large-, intermediate- and small-scale modes, characterised by their horizon entries. A mode enters the horizon when the comoving horizon is comparable to the wavelength, i.e. when $k\eta(x) \gtrsim 1$. We let $k_{\rm eq} = 1/\eta(x_{\rm eq})$ to separate the modes entering the horizon before and after matter-radiation equality $x_{\rm eq}$. The hierarchy of modes is summarised below.

- Small-scale modes: $k \gg k_{\rm eq}$, horizon entry during radiation domination.
- Intermediate-scale modes: $k \sim k_{\rm eq}$, horizon entry around the time of matter-radiation equality.
- Large-scale modes: $k \ll k_{\rm eq}$, horizon entry during matter domination.

The comoving scales remain constant in time. When the modes are far outside the horizon ($k\eta \ll 1$), what we refer to as the "super-horizon regime", perturbations have not yet entered the horizon. Together with the assumption that the early universe is optically thick and rapidly rarefying ($\tau, |d\tau/dx| \gg 1$), very useful physical approximations can be employed to find a set of equations connecting the initial conditions of our quantities. For the full set, see appendix B.3.

4.1.1. Metric perturbations

The FRW metric from Eq. (1) describes a smooth universe, meaning a universe whose background is homogeneous and isotropic. A first order linear perturbation to the metric can be applied through

$$g_{\mu\nu} = g_{\mu\nu}^{(0)} + \delta g_{\mu\nu}; \quad \left| \delta g_{\mu\nu} \right| \ll 1, \tag{44}$$

where $g_{\mu\nu}^{(0)}$ is the zeroth order term—the FRW metric.[3] We will work the so-called conformal-Newtonian gauge, where the perturbation $\delta g_{\mu\nu}$ is given in terms of the potentials Ψ and Φ. The resulting perturbed metric now reads

$$ds^2 = e^{2x} \left[-(1 + 2\Psi) \, d\eta^2 + (1 + 2\Phi) \, \delta_{ij} \, dx^i \, dx^j \right]. \tag{45}$$

The time-dependent gravitational potential is encoded in Ψ in the sense that it measures how the strength of the gravitational field in the perturbed universe differs from that of the smooth one. Φ describes the spatial curvature of the universe as it is a measure of the deviation of the spatial curvature from the smooth background. Both scalar perturbations are related to the distribution of matter in the universe. These fundamental quantities are the

---

[2] Solving it directly is highly non-trivial.

[3] We use the term "metric" on both $g_{\mu\nu}$ and $ds^2 = g_{\mu\nu} \, dx^\mu \, dx^\nu$.

ones from which we will express the initial conditions of the system.

It is the Poisson equation that determines the evolution of Φ. The sum $\Phi + \Psi$ is given by an equation for anisotropic stress, resulting in a dynamical expression for Ψ. The equations are given in appendix B.1, Eq. (B.1).

The absence of anisotropic stress causes $\Phi = -\Psi$. Shear stress in a tightly coupled fluid is manifestly absent; only anisotropic motion of fluid particles gives rives to non-zero terms in the stress tensor. We therefore use this to set the initial condition on Φ (Eq. (B.5a)). In addition, we expect to see that $\Psi + \Phi \simeq 0$ before recombination for large-scale modes $k \lesssim k_{\mathrm{eq}}$. For small-scale modes, fluctuations in the primordial plasma were large and gave rise to oscillating gravitational potentials.

The initial condition for Ψ comes from inflation. In Dodelson & Schmidt (2021) it is explained how this quantity is proportional to the curvature perturbation $\mathcal{R}$ immediately after inflation, and that this $\mathcal{R}$ is conserved in the super-horizon regime. In particular, the value of Ψ post inflation is $\Psi_{\mathrm{init}} = -2/3\mathcal{R}$. The value of $\mathcal{R}$ depends on the inflationary model one uses, and is for our purposes, essentially a question of normalisation. The simplest choice of $\mathcal{R} = 1$ is the one we will use.

4.1.2. Matter perturbations

The normal matter in the universe is either cold dark or baryonic. We set the perturbed number densities of these species to be

$$n_s = n_s^{(0)} [1 + \delta_s] ; \quad s = \mathrm{c}, \mathrm{b}, \tag{46}$$

so that $n_s^{(0)} \delta_s$ is the leading order term. To zeroth order, we have $n_s^{(0)} \propto \mathrm{e}^{-3x}$ from the Boltzmann equation. This is equivalent to perturbing the time-time-component of the energy momentum tensor,

$$T_{00} = T_{00}^{(0)} + \delta T_{00} = -\rho_s (1 + \delta_s). \tag{47}$$

We denote the fluid (or "bulk") velocity of a species s as $\boldsymbol{u}_s$, and its speed as u_s. We consider longitudinal velocities such that

$$\boldsymbol{u}_s = \boldsymbol{u}_s(x, \boldsymbol{k}) = u_s(x, \boldsymbol{k}) \frac{\boldsymbol{k}}{k}. \tag{48}$$

In addition, we use the convention that $u_s \to i u_s$.

The governing equation for δ_s is the continuity equation for n_s to first order. This takes the same form for $s = \mathrm{c}$ and $s = \mathrm{b}$. In general, for species s,

$$\frac{\mathrm{d}\delta_s}{\mathrm{d}x} = (1 + w_s) \left(\frac{ck}{\mathcal{H}} u_s - 3 \frac{\mathrm{d}\Phi}{\mathrm{d}x} \right), \tag{49}$$

with w_s as before. For normal matter, $w_{\mathrm{m}} = w_{\mathrm{c}} = w_{\mathrm{b}} = 0$, whereas for relativistic particles we have $w_{\mathrm{r}} = w_\gamma = w_\nu = 1/3$.

The equation for u_s, the Euler equation, differs by one term for baryons and CDM. The collision-less Euler equation reads

$$\frac{\mathrm{d}u_s}{\mathrm{d}x} = -(1 - 3c_s^2) u_s - \frac{w_s ck}{(1 + w_s)\mathcal{H}} \delta_s - \frac{ck}{\mathcal{H}} \Psi, \tag{50}$$

where c_s is the sound speed. $c_s^2 = w_{\mathrm{m}}$ for baryons and CDM and $c_s^2 = w_{\mathrm{r}}$ for photons and neutrinos. In contrast with CDM, baryons interact with photons, giving rise to an additional term

$$\text{momentum transfer} = -\frac{4\Omega_\gamma}{3\Omega_{\mathrm{b}}} \frac{\mathrm{d}\tau}{\mathrm{d}x} \left(u_\gamma - u_{\mathrm{b}} \right) = -\frac{\mathrm{d}\tau}{\mathrm{d}x} \frac{u_\gamma - u_{\mathrm{b}}}{R}, \tag{51}$$

where $R = R(x)$ is the baryon-to-photon energy ratio as before (see Eq. (36)).

The final differential equations for the density and velocity perturbations are given in appendix B.1, Eq. (B.2).

Without anticipating the course of events too much, we state that the initial conditions for the matter perturbations (appendix B.3, Eq. (B.5)) follow from their relation to the photons' velocity and density perturbations, and the assumption that perturbations are adiabatic:

$$(1 + w_{s'})\delta_{s'} = (1 + w_s)\delta_s$$
$$u_{s'} = u_s \tag{52}$$

4.1.3. Temperature fluctuations

We let the momentum of a photon be $\boldsymbol{p}$ and its magnitude $p = |\boldsymbol{p}|$. Define $\mu \equiv (kp)^{-1} \boldsymbol{k} \cdot \boldsymbol{p}$. The perturbed photon temperature T_γ is

$$T_\gamma = T_\gamma^{(0)} [1 + \Theta(\mu)], \tag{53}$$

where $T_\gamma^{(0)} = T_{\mathrm{CMB0}} \mathrm{e}^{-x}$. The photon perturbation $\Theta(\mu)$ can be expanded into multipoles Θ_ℓ. The relation is

$$\Theta_\ell = \frac{\mathrm{i}^\ell}{2} \int_{-1}^1 \mathrm{d}\mu \, \mathcal{P}_\ell(\mu)\Theta(\mu) \iff \Theta(\mu) = \sum_{\ell=0}^{\infty} \frac{2\ell + 1}{\mathrm{i}^\ell} \Theta_\ell \mathcal{P}_\ell(\mu), \tag{54}$$

where $\mathcal{P}_\ell(\mu)$ are the Legendre polynomials. The hierarchy of differential equations governing the temperature multipoles are presented in appendix B.1, Eq. (B.3).

If we study the differential equations for the first two moments in Eq. (B.3c), we can identify the former as the continuity equation for the perturbed photon density by setting $\delta_\gamma = 4\Theta_0$,

$$\frac{\mathrm{d}\delta_\gamma}{\mathrm{d}x} = \frac{4}{3} \left(\frac{ck}{\mathcal{H}} - 3 \frac{\mathrm{d}\Phi}{\mathrm{d}x} \right), \tag{55}$$

exactly Eq. (49) with $s = \gamma$. The equation for the dipole serves as the perturbed Euler equation, Eq. (56), if we let the longitudinal component of the photon velocity be $u_\gamma = -3\Theta_1$, that is

$$\frac{\mathrm{d}u_\gamma}{\mathrm{d}x} = -\frac{ck}{4\mathcal{H}} \delta_\gamma + \frac{2ck}{\mathcal{H}} \Theta_2 - \frac{ck}{\mathcal{H}} \Psi + \frac{\mathrm{d}\tau}{\mathrm{d}x} \left[u_\gamma - u_{\mathrm{b}} \right]. \tag{56}$$

The last term—the momentum transfer—ensures that photons and baryons behave as a single fluid early on when Compton scattering is efficient. We refer to this period as "the tight coupling regime". As this is true for all scales in the early radiation dominated universe, we could get the initial conditions for the first two multipoles from $\delta_\gamma = 3/4\delta_{\mathrm{b}}$ and $u_\gamma = u_{\mathrm{b}}$. However, we will instead go the other way around and use Θ_0 and Θ_1 to set the initial conditions for the matter perturbations. In the radiation-dominated era and super-horizon regime, a reasonable approximation to $\mathrm{d}\Phi/\mathrm{d}x$ in Eq. (B.1a) is $\Psi + 2\Theta_0$. This derivative is assumed to be very small in the early stages for all modes, so by setting this to zero, we get the initial value of the monopole. In Dodelson & Schmidt (2021, Eq. (7.95)) it is stated what value Θ_1 takes at the beginning, which is what we use in appendix B.3.

The monopole in the CMB temperature anisotropy power spectrum, Θ_0, is the average temperature of the CMB sky and is the same for any observer moving with the Hubble flow. The dipole term Θ_1 corresponds to the temperature anisotropy resulting from our galaxy's motion with respect to the CMB rest frame (the Doppler effect). Arising from the variations across the CMB sky is the quadrupole, Θ_2. Higher multipoles correspond to increasingly smaller angular scales. We therefore argue that

$$|\Theta_0| \gg |\Theta_1| \gg |\Theta_2| \gg |\Theta_3| \gg \cdots. \tag{57}$$

4.1.4. Tight coupling

Due to numerical obstacles, we cannot use the full set of equations from appendix B.1 in the tight coupling regime. As $u_b \simeq u_\gamma = -3\Theta_1$ in this period, and $|\mathrm{d}\tau/\mathrm{d}x|$ is very large at this time, the last term in Eq. (56) is unfortunate. The same factor appears in the continuity equation for baryons (Eq. (51)). The good news is that in this regime, some very useful approximations are viable, eventually allowing us to replace the differential equations for u_b and Θ_2 with differential equations that are way more numerically friendly. We present these in appendix B.2.

We assume tight coupling to begin in the very early universe and prolong until no later than recombination. The following three equations shall hold throughout the regime:[4]

$$\left| \frac{\mathrm{d}\tau(x)}{\mathrm{d}x} \right| > 10 \tag{58a}$$

$$\left| \frac{\mathrm{d}\tau(x)}{\mathrm{d}x} \right| > 10 \frac{ck}{\mathcal{H}(x)} \tag{58b}$$

$$x \leq -8.3 \tag{58c}$$

The higher moments of the temperature fluctuations are very small in this regime ($|\Theta_{\ell \geq 2}| \ll 1$), and we can use the semi-analytical recursive relations in Eq. (B.7). However, we will not bother to compute others than Θ_2, as this is the only one our set of equations rely on. As we will see, there is a much cleverer way of obtaining the higher order multipoles, if our overall goal is to study today's values.

The relations in question show up when setting $\mathrm{d}\Theta_\ell/\mathrm{d}x \to 0$ and using $|\Theta_{\ell+1}| \ll |\Theta_\ell|$ in Eq. (B.3c).

4.1.5. Line-of-sight integration

Callin (2006) explains how one can relate the current value of the temperature multipoles $\Theta_\ell(x=0, k)$ to the temperature source function $\tilde{S}(x, k)$ and spherical Bessel functions

$$j_\ell(z) = \frac{i^\ell}{2} \int_1^{-1} \mathrm{d}\mu \, \mathcal{P}_\ell(\mu) e^{-i\mu z}, \tag{59}$$

eventually obtaining

$$\Theta_\ell(x=0, k) = \int_{-\infty}^{0} \mathrm{d}x' \, \tilde{S}(x', k) \cdot j_\ell(k[\eta_0 - \eta(x')]). \tag{60}$$

The full expression for $\tilde{S}(x, k)$ is found in appendix C, but we stress its dependence on Θ_2.

Using this so-called line-of-sight integration method, it seems we can compute all $\Theta_{\ell > 2}$ given $\Theta_{\ell \leq 2}$. However, after tight coupling, the evolution of a multipole Θ_ℓ depends on both $\Theta_{\ell-1}$ and $\Theta_{\ell+1}$. That is to say, to compute Θ_2, we need Θ_3 for which we need Θ_4, and so on. The Boltzmann hierachy cutoff provides a solution to this apparent issue. The method allows us to only include $\ell = 0, 1, \ldots, \ell_{\max} \sim 6\text{–}8$ when solving the differential equations in Eq. (B.3) by treating $\Theta_{\ell_{\max}}$ slightly different than $\Theta_{\ell < \ell_{\max}}$.

4.2. Implementation details

We extended our C++ program to account for perturbations in order to study the evolution of structure in the universe. Objects of the classes from Sect. 2.2 and Sect. 3.2 was sufficient for the newest class to do all the desired work.

---

[4] $x = -8.3$ used as a "fair while before the onset of recombination".

The following recipe (i) – (vi) was used for each of the 200 logarithmically spaced values $k \in [k_{\min}, k_{\max}]$, where $k_{\min} = 5 \times 10^{-5}$ Mpc^{-1} and $k_{\max} = 3 \times 10^{-1}$ Mpc^{-1}. In the full regime, we used $\ell_{\max} = 7$.

(i) For the initial time x_{init}, set the initial conditions according to appendix B.3 (Eq. (B.5) and (B.6)).
(ii) Compute the time for which tight coupling ends, $x_{\mathrm{tc,end}}(k)$. That is, find the x for which Eq. (58a), (58b) and/or (58c) is violated.
(iii) Solve the set of differential equations from appendix B.2 using RK4(−6, −8, −8). Integrate from $x = x_{\mathrm{init}}$ to $x = x_{\mathrm{tc,end}}(k)$.
(iv) Use the result from the tight coupling regime at $x = x_{\mathrm{tc,end}}(k)$ to set the initial conditions for the full system. The higher multipoles (up to $\ell = \ell_{\max}$) are set according to Eq. (B.7) with $x = x_{\mathrm{tc,end}}(k)$.
(v) Solve the set of differential equations from appendix B.1 using RK4. Integrate from $x = x_{\mathrm{tc,end}}(k)$ to $x = 0$.
(vi) Sew solutions together and save result.

The expression for $\tilde{S}(k, x)$ as provided in appendix C was implemented succeeding a successful computation of the perturbations.

4.2.1. Parallelisation

The set of equations is completely decoupled in k, making our main problem highly parallelisable. Very few, very simple lines were added to code to execute (i) – (vi) in parallel using shared-memory parallelisation according to the *OpenMP* standard.

4.3. Results

From this point (Sects. 4 & 5), the results were obtained *after* reproducing the background with $N_{\mathrm{eff}} = 0$. This caused some changes in numerical values for e.g. matter-radiation equality, but did not change the important results and takeaways from the previous work (Sects. 2 & 3).

The figures below demonstrate our results for three wave numbers $k \in \{k_l, k_i, k_s\}$. We chose $k_l \equiv 0.001$ Mpc^{-1} to represent the large-scale modes and $k_s \equiv 0.1$ Mpc^{-1} for the small-scales. The intermediate-scale modes are represented by $k_i \equiv 0.01$ Mpc^{-1}. We noted that $k_i \approx k_{\mathrm{eq}} = 0.0115$ Mpc^{-1}. For relevant details, see Table 3. We stress that the time of horizon entry is merely a definition, and is at best a naive estimate of when a mode succumbs to causal physics.

We present the absolute values of the matter and energy perturbations in the upper panels of Fig. 9. The lower panels of said figure emphasise the oscillations around zero of the density and velocity perturbations for the photons.

The photon quadrupole is plotted in Fig. 10. Note that the x-axis is relatively short in this plot, as the function is flat until $x \sim -9$.

Fig. 11 shows the scalar potentials as functions of time. The upper panel shows only the perturbation to the time-part of the metric, whereas the lower panel shows the sum of this and the spatial perturbation.

Note that we completely dismissed neutrinos and photon polarisation. That is, we sat the effective neutrino number to be zero, slightly changing the background from Sect. 2.

The end of tight coupling turned out to be $x_{\mathrm{tc,end}}(k) = -8.3$ for all three wavenumbers. The three modes k_s, k_i and k_l entered the horizon at $x \sim -11$, -8.5 and -5.2, respectively. That is, k_s enters the horizon in the radiation-dominated era, k_i just around
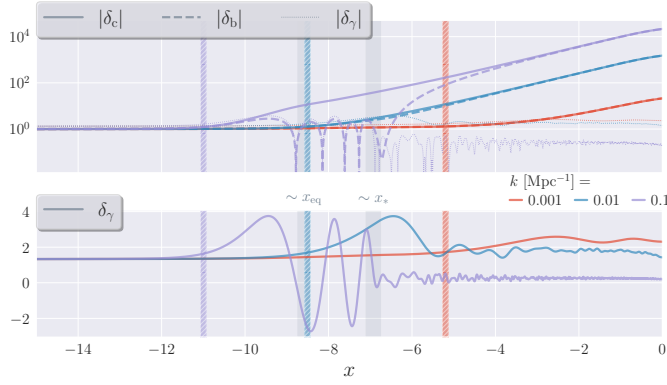
(a) Density perturbations $\delta_s(x,k)$ for $s = c, b$ and γ meaning cold dark matter, baryons and photons, respectively. Recall that $\delta_\gamma(x,k) = 4\Theta_0(x,k)$.
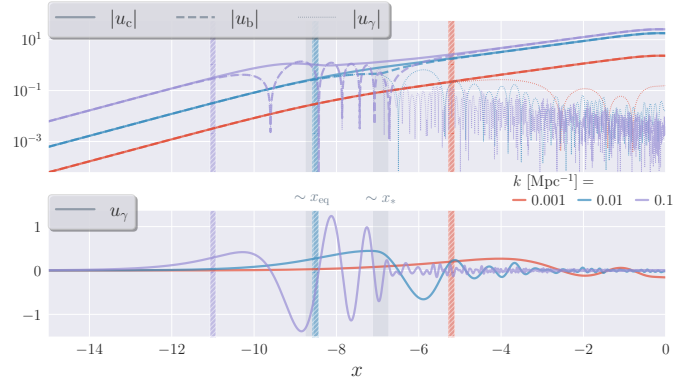
(b) Velocity perturbations $u_s(x,k)$ for $s = c, b$ and γ meaning cold dark matter, baryons and photons, respectively. Recall that $u_\gamma(x,k) = -3\Theta_1(x,k)$.

Fig. 9: Matter perturbations to normal matter and photons as functions of logarithmic expansion x for three wavenumbers k. The time of radiation-matter equality is empasized by a shaded grey region, as is the recombination. Horizon entries are shown as thick, vertical coloured lines. The upper panels show the absolute value of the quantities in question with a logarithmic y-axes, whereas the lower panels show the actual quantity for the photons only.
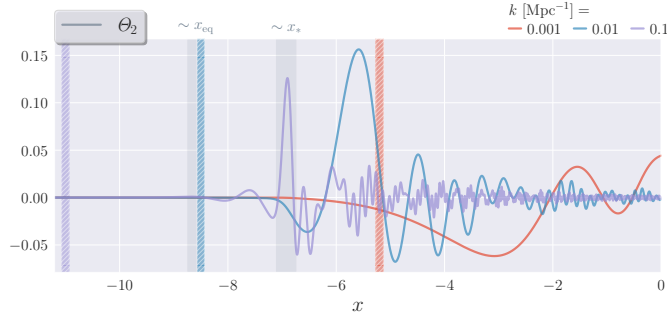
Fig. 10: The graphs show the photon quadrupole $\Theta_2(x,k)$ as function of logarithmic scale factor x for three different wavenumbers k. The shaded grey regions represent the epochs of radiation-matter equality and receombination. Horizon entries are shown as thick, vertical coloured lines.
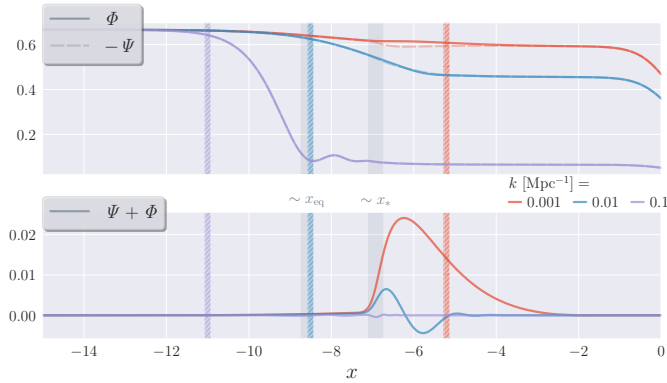
Fig. 11: The graphs show the metric perturbations as functions of logarithmic scale factor x for three different wavenumbers k. The shaded grey regions represent the epochs of radiation-matter equality and receombination. Horizon entries are shown as thick, vertical coloured lines. Upper panel: spatial curvature fluctuation $\Phi(x,k)$ and the negative of the gravitational potential $-\Psi(x,k)$. Lower panel: sum of the two potentials $(\Psi + \Phi)(x,k)$.

the matter-radiation equality and k_l enters when the universe is dominated by matter (see Fig. 1; only now $x_{eq} = -8.66$). We de-

cided to present updated details about the comoving wavenumbers we consider in a table; Table 3.

Table 3: The comoving wavenumbers we address, with their time of horizon entry (rightmost column).

	k [Mpc^{-1}]	$k/k_1{}^a$	$x \mid k\eta(x) \overset{!}{=} 1$
k_l ($\leadsto$ large scales)	0.001	0.052	-10.98
k_i ($\leadsto$ intermediate scales)	0.01	0.52	-8.490
k_s ($\leadsto$ small scales)	0.1	5.2	-5.182
k_{eq} ($\Rightarrow$ equality scale)	0.0115	0.60	-8.658
Sound horizon at decoupling:			$s_* = 164.0$ Mpc
Comoving distance at decoupling:			$\chi_* = 13.94$ Gpc
Fundamental mode:[a]			$k_1 = 191.6$ Gpc^{-1}
Fundamental tone:[b]			$\ell_{pk} \approx 267$

Notes. The top panels show useful dimesions for the modes we consider. The bottom panel lists values that will be useful when analysing and predicting the results. All values are computed with $N_{eff} = 0$.
[a] $k_1 \equiv \pi/s_*$ is the fundamental Fourier mode. [b] $\ell_{pk} \equiv \chi_* k_1$ is related to the (loosely defined) fundamental tone $\ell_1 \approx \ell_{pk}$, which locates the first peak of the CMB power spectrum.

4.4. Discussion

What was not discussed too much in Sect. 4.1, was the physics of the acoustic oscillations and how they are frozen in at decoupling. We shall study these mechanisms in more detail in Sect. 5.1. However, we choose to consider some of these concepts when discussing the results in this section, hoping that the statements will be justified later on.

To summarise the discussion below, cosmic perturbations exhibit scale-dependent behaviour, with different physical processes dominating on large and small scales. Our results are consistent with expectations based on standard cosmological models and provide valuable insight into the growth of structure in the universe.

Matter perturbations The upper panels of Fig. 9 show that only the small-scale modes experience oscillations in the baryonic matter perturbations. Modes on larger scales than this enter the horizon too late to be affected by the causal physics that is the interplay between the radiation pressure and the gravitational force in the photon-baryon plasma—that which gives rise to the acoustic oscillations. The adiabatic initial conditions make sure the normal matter perturbations are the same for CDM and baryons in the beginning and cease to be the same in the end, for all modes. Although for large-scale modes, these species never decouple at all since horizon entry happens in proper matter domination. Shortly after the onset of recombination, sub-horizon baryonic matter falls into CDM potential wells, demonstrated by the baryon overdensities during the end of the Compton drag epoch (i.e. $\delta_b(x \approx x_*, k = k_s, k_i)$ in Fig. 9a).

In Fig. 9a, we observe that the overdensities of (non-interacting) cold dark matter inside the horizon grows exponentially in the matter dominated era. During radiation domiation, the sub-horizon CDM overdensity, $\delta_c(x, k_s)$, grows even faster. On super-horizon scales, the CDM overdensities are are constant, as a result of our gauge choice.[5] In addition, we can see that the overdensities flatten out as we enter the DE dominated era ($x_\Lambda \approx -0.026$), which is expected from the SW effect.

In the fully recomined universe as well as on super-horizon scales, the baryonic matter perturbations reduce to those of dark matter. This is not completely accurate for $\delta_b(x \gtrsim x_*, k_s)$, c.f. Fig. 9a, upper panel. Here, the state at which the mode k_s is caught in at recombination, is "just starting is sixth decompression" since $k_s \approx 5.2k_1$, c.f. Table 3 (or simply count compressions and decompressions in $\Theta_0(x < x_*, k_s)$).

Even though k_i is inside the horizon at $x = x_*$, it does not probe baryonic acoustic oscillations (BAOs) as the fluid system is only half-way to its first extremum.

We spot indications of *baryon loading* in the lower panel of Fig. 9a. This concept will be introduced in Sect. 5.1.2.

Photon temperature perturbations The tight coupling between photons and baryons is evident from their respective velocity graphs in th upper panel of Fig. 9b. For the sub-horizon modes (k_s and k_l), the photon velocity starts deviating from the baryon velocity during recombination, at which the high-frequency photon starts rattling around before it streams freely in the universe.

On large scales, the bulk velocities are suppressed due to adiabatic initial conditions, while on small scales, they are enhanced due to gravitational collapse. The bulk velocity for photons undergoes oscillations due to the same acoustic physics as the photon overdensity.

We also observe the approximate time of horizon crossing for the different wavenumbers, which we see as the time when the photon velocity starts deviating from the velocity of the cold dark matter.

Finally, we observe that for all modes, as they enter the horizon, they first compress ($d\delta_\gamma/dx > 0$, $u_\gamma > 0$) once before decompressing, then compressing again, and so on.

The quadrupole moment $\Theta_2(x, k)$ in Fig. 10 exhibits oscillatory behaviour on all scales due to the same acoustic physics as the photon overdensity and bulk velocity. For small-scale modes, the amplitude of the oscillations is suppressed as photons diffuse from overdense regions. This is an example of *diffusion damping* that will be discussed later.

Metric perturbations We make a note of the fact that the curvature perturbation is essentially a perturbation to the expansion factor, $\Phi \cong \delta a/a$. In the upper panel of Fig. 11, we study the scalar potential of the mode that enters the horizon during the radiation-dominated era, $\Phi(x, k = k_s)$. Horizon entry provokes the growth of matter perturbations and the potential drops. This is because radiation has pressure and therefore does not manage to cluster enough to fight the universe's expansion and keep the potentials up. As matter starts to dominate radiation, the propagating acoustic wave (in real space) generated by the oscillating baryonic matter (in Fourier space) is imprinted in the gravitational potential. We see this as the oscillations starting at $x \sim x_{eq}$ in Fig. 11.

Variations gravitational potentials exhibit large-scale physical effects and therefore also affect super-horizon scales. Around $x \sim x_{eq}$ expansion is affected by radiation and matter alike, resulting in decaying gravitational potentials up until any residual radiation has vanished, where they flatten out. The fact that the baryon fraction Ω_{b0}/Ω_{m0} is substantial manifests in the further decay of the potentials between radiation-matter equality and the end of the Compton drag epoch, due to their inability to cluster below the sound horizon. Intermediate scales experience more or less the same potential evolutions as large scales. We can see how the DE at late times accelerates the expansion and causes large-scale potential wells/hills to decay (c.f. $\Phi(x \gtrsim x_\Lambda, k = k_i, k_l)$).

As a side note, the lower panel shows a plot of $\propto -\Theta_2(x, k)/k^2 \cdot e^{-2x}$ (see Eq. (B.1b)). After recombination, the anisotropic stress becomes non-zero, and so does the sum $(\Psi + \Phi)(x, k)$ for all scales, as we anticipated. Tiny fluctuations are visible before this for the small-scale mode. [6]

5. CMB and matter power spectra

Quantum fluctuations from the early universe generates inhomogeneity in the form of (energy) density enhancements and deficits. The rapid expansion during inflation stretches these quantum fluctuations to cosmic scales. From this, local fluctuations in the gravitational potential are implied. The primordial plasma compresses in potential wells found in regions of high density. Analogously, the tightly coupled plasma rarefies in potential hills created in regions of low density. These mechanisms generate pressure waves propagating at the speed of sound, eventually imprinting a pattern of sound in the CMB temperature. Unless otherwise stated, compressions and decompressions in a fluid are seen from the point of view of the potential *well*.

Where the fluid is compressed in a well and thus heated, there is a region *nearby*[7] where the fluid expands on a hill and cools down. It its convenient to decompose the fluctuations into plane wave-modes that evolve independently, as we did in Sect. 4. Now, if such a mode corresponds to a wavelength that is shorter than the particle horizon, *and* the photons are tightly coupled to the baryons, the temperature fluctuation will oscillate in time as the fluid compresses and rarefies. At recombination, sound waves stop oscillating and are frozen in. The last scattering surface corresponds to a maximal length for these sound waves to have travelled; the sound horizon at decoupling, briefly mentioned in Sect. 3. There is then a mode (k_1) that had just enough time to compress once, necessarily with half a wave-

---

[5] $\delta_c(x, k \ll \mathcal{H}) \propto \mathcal{R}|_{k \ll \mathcal{H}}$ = constant in the Newtonian gauge.

[6] Most evident when scaling the graphs with the wavenumber, e.g. $k^{3/2}(\Psi + \Phi)$.

[7] Near enough to be in causal contact with the aforementioned density enhancement.

length equal this distance. The mode (k_2) with the this distance as its whole wavelength, will have completed one cycle of compression/decompression at decoupling. These modes (2π over comoving wavelength) are then $k_n = n\pi/s_*$, where $n \in \mathbb{N}$ by extension.

Now, the perturbations from Sect. 4 can be combined with an estimate of the post-inflation dilated quantum fluctuations to form theoretical power spectra, in particular those of the photon temperature and non-relativistic matter today. We will in this section produce these observables using the simplest concordance model of inflation.

5.1. Theory

The power spectrum, denoted $P(\boldsymbol{k})$, is defined as the Fourier transform of the two-point correlation function, denoted $\xi(\boldsymbol{x})$. That is

$$\xi(\boldsymbol{x}) = \int \frac{d^3 k}{(2\pi)^3} e^{i\boldsymbol{k}\cdot\boldsymbol{x}} P(\boldsymbol{k}), \tag{61}$$

and by performing a Henkel transform we get

$$\xi(r) = \int dk \frac{k^2}{2\pi^2} \frac{\sin(kr)}{kr} P(k) = \int \frac{dk}{k} \frac{\sin(kr)}{kr} \frac{k^3 P(k)}{2\pi^2}, \tag{62}$$

where $r = |\boldsymbol{x}|$. By a similar line of thought, we can relate the angular power spectrum $C(\ell)$ in harmonic space to the correlation between to points on the sky separated by an angle θ through

$$\xi(\theta) = \frac{1}{4\pi} \sum_\ell \sum_{m=-\ell}^{\ell} \langle |a_{\ell m}|^2 \rangle = \frac{1}{4\pi} \sum_\ell (2\ell + 1) C(\ell) \mathcal{P}_\ell(\mu), \tag{63}$$

where $\mu = \cos\theta$.

Notational note To not be overwhelmed by notation in this section, we let t be the time variable in real space and x the time variable in Fourier space, such that in general,

$$f(t, \boldsymbol{x}) = \int \frac{d^3 k}{(2\pi)^3} f(x, \boldsymbol{k}). \tag{64}$$

We will also account for the primordial fluctuations by setting $f(x, \boldsymbol{k}) = f(x, k)\mathcal{R}(\boldsymbol{k})$, where $f(x, k)$ is a computed perturbation quantity from Sect. 4. To be very clear, $x \neq |\boldsymbol{x}|$.

Power spectra We revisit the curvature perturbation $\mathcal{R}(\boldsymbol{k})$ immediately after inflation, that which determines the initial conditions for each Fourier mode. During the generation of fluctuations, there should be no preferred position nor direction in space, resulting in statistical homogeneity and isotropy of said fluctuations. We let $\langle \cdot \rangle$ denote the statistical expectation value over many realisations of the universe. Thus, the primordial power spectrum $P_\mathcal{R}(k)$ is given by

$$\langle \mathcal{R}(\boldsymbol{k})\mathcal{R}^*(\boldsymbol{k}') \rangle = (2\pi)^3 \delta(\boldsymbol{k} - \boldsymbol{k}') P_\mathcal{R}(k). \tag{65}$$

The inflationary model we consider predicts the dimensionless primordial power spectrum

$$\Delta^2_\mathcal{R}(k) = \frac{k^3}{2\pi^2} P_\mathcal{R}(k) = \mathcal{A}_{\rm s} \left(\frac{k}{k_{\rm p}} \right)^{n_{\rm s}-1}, \tag{66}$$

where $\mathcal{A}_{\rm s}$ is the primordial amplitude, $n_{\rm s}$ the scaler spectral index and $k_{\rm p}$ a fundamental pivot scale.

Further, we assume fluctuations to be gaussian. The perturbations are adiabatic and their averages vanish. Now, the power spectrum of perturbation variable f is the combination between the initial power spectrum and a deterministic transfer function f^2:

$$\langle f(x, \boldsymbol{k}) f^*(x, \boldsymbol{k}') \rangle = f(x, k) f^*(x, k') \langle \mathcal{R}(\boldsymbol{k})\mathcal{R}^*(\boldsymbol{k}') \rangle$$
$$= (2\pi)^3 \delta(\boldsymbol{k} - \boldsymbol{k}') |f(x, k)|^2 P_\mathcal{R}(k) \tag{67}$$

For a field on a 3D sphere $g(\hat{\boldsymbol{n}})$, we can expand the directional dependence in spherical harmonics,

$$g(\hat{\boldsymbol{n}}) = g(t, \boldsymbol{x}, \hat{\boldsymbol{n}}) = \sum_\ell \sum_{m=-\ell}^{\ell} a_{\ell m}(t, \boldsymbol{x}) Y_{\ell m}(\hat{\boldsymbol{n}}), \tag{68}$$

and the (angular) power spectrum $C(\ell)$ today is given by

$$\langle a_{\ell m}(t_0, \boldsymbol{x}) a^*_{\ell' m'}(t_0, \boldsymbol{x}) \rangle = \delta_{\ell\ell'} \delta_{mm'} C(\ell). \tag{69}$$

5.1.1. The CMB power spectrum

We begin by expanding the temperature perturbation $\Theta(t, \boldsymbol{x}, \hat{\boldsymbol{p}})$ into spherical harmonics, as in Eq. (68). The orthogonality of $Y_{\ell m}(\hat{\boldsymbol{p}})$[8] gives the coefficients

$$a_{\ell m} = a_{\ell m}(t, \boldsymbol{x}) = \int d\Omega_{\hat{\boldsymbol{p}}} Y^*_{\ell m}(\hat{\boldsymbol{p}}) \Theta(t, \boldsymbol{x}, \hat{\boldsymbol{p}}), \tag{70}$$

where $d\Omega_{\hat{\boldsymbol{p}}} = \sin\vartheta\, d\vartheta\, d\varphi$ is the infinitesimal solid angle element of $\hat{\boldsymbol{p}} = (\vartheta, \varphi)$. Further, we expand the coefficients into Fourier modes and multipoles:

$$a_{\ell m} = \int d\Omega_{\hat{\boldsymbol{p}}} Y^*_{\ell m}(\hat{\boldsymbol{p}}) \int \frac{d^3 k}{(2\pi)^3} e^{i\boldsymbol{k}\cdot\boldsymbol{x}} \Theta(x, \boldsymbol{k}, \hat{\boldsymbol{p}})$$
$$= \int d\Omega_{\hat{\boldsymbol{p}}} Y^*_{\ell m}(\hat{\boldsymbol{p}}) \int \frac{d^3 k}{(2\pi)^3} e^{i\boldsymbol{k}\cdot\boldsymbol{x}} \sum_{\ell'} \frac{2\ell'+1}{i^{\ell'}} \mathcal{P}_{\ell'}(\mu) \Theta_{\ell'}(x, \boldsymbol{k})$$
$$\tag{71}$$

In the second line, we used that $\mu = \hat{\boldsymbol{p}} \cdot \hat{\boldsymbol{k}}$ ($\hat{\boldsymbol{k}} \equiv \boldsymbol{k}/k$) to let $\Theta(x, \boldsymbol{k}, \hat{\boldsymbol{p}}) \to \Theta(x, \boldsymbol{k}, \mu)$. Taking the ensemble average $\langle a_{\ell m} a^*_{\ell' m'} \rangle$ will only affect the $\Theta_{\ell'}(x, \boldsymbol{k})$'s in the expression above, as this depends on the initial amplitude of a mode. As initially explained, we reintroduce the curvature perturbation $\mathcal{R}(\boldsymbol{k})$ by substituting $\Theta_\ell(x, \boldsymbol{k}) \to \Theta_\ell(x, k)\mathcal{R}(\boldsymbol{k})$, where $\Theta_\ell(x, k)$ are the perturbations we computed in Sect. 4. We get the only relevant average distribution:

$$\langle \Theta_\ell(x, \boldsymbol{k}) \Theta^*_{\ell'}(x, \boldsymbol{k}') \rangle \to \Theta_\ell(x, k) \Theta^*_{\ell'}(x, k') \langle \mathcal{R}(\boldsymbol{k})\mathcal{R}^*(\boldsymbol{k}') \rangle;$$
$$\langle \mathcal{R}(\boldsymbol{k})\mathcal{R}^*(\boldsymbol{k}') \rangle = (2\pi)^3 \delta(\boldsymbol{k} - \boldsymbol{k}') P_\mathcal{R}(k) \tag{72}$$

Writing it out, we get

$$\langle a_{\ell m} a^*_{\ell' m'} \rangle = \int d\Omega_{\hat{\boldsymbol{p}}} \int d\Omega_{\hat{\boldsymbol{p}}'} Y^*_{\ell m}(\hat{\boldsymbol{p}}) Y_{\ell' m'}(\hat{\boldsymbol{p}}')$$
$$\cdot \int \frac{d^3 k}{(2\pi)^3} P_\mathcal{R}(k) \sum_{\ell_1 \ell_2} (2\ell_1 + 1)(2\ell_2 + 1)(-i)^{\ell_1 - \ell_2}$$
$$\cdot \mathcal{P}_{\ell_1}(\mu) \mathcal{P}_{\ell_2}(\mu') \Theta_{\ell_1}(x, k) \Theta^*_{\ell_2}(x, k), \tag{73}$$

---

[8] $\int d\Omega_{\hat{\boldsymbol{n}}} Y_{\ell m}(\hat{\boldsymbol{n}}) Y^*_{\ell' m'}(\hat{\boldsymbol{n}}) = \delta_{\ell\ell'} \delta_{mm'}$.

where we used the Dirac-Delta function from Eq. (72) to eliminate $\int d^3k' (2\pi)^{-3} e^{i(k-k')\cdot x}$. The identity

$$\int d\Omega_{\hat{p}} Y_{\ell m}(\hat{p}) \mathcal{P}_{\ell'}(\hat{k} \cdot \hat{p}) = \delta_{\ell\ell'} \frac{4\pi}{2\ell+1} Y_{\ell m}(\hat{k}) \tag{74}$$

gives rise to factors $\delta_{\ell\ell_1}$ and $\delta_{\ell'\ell_2}$, killing the infinite sums in Eq. (73). We are left with

$$\langle a_{\ell m} a_{\ell' m'}^* \rangle = (4\pi)^2 \int \frac{d^3k}{(2\pi)^3} Y_{\ell m}^*(\hat{k}) Y_{\ell' m'}(\hat{k}) \Theta_\ell(x,k) \Theta_{\ell'}^*(x,k) P_{\mathcal{R}}(k). \tag{75}$$

Spherical symmetry $(d^3k \to k^2 dk d\Omega_{\hat{k}})$ gives

$$\langle a_{\ell m} a_{\ell' m'}^* \rangle = \frac{2}{\pi} \int d\Omega_{\hat{k}} Y_{\ell m}^*(\hat{k}) Y_{\ell' m'}(\hat{k}) \int dk\, k^2 \Theta_\ell(x,k) \Theta_{\ell'}^*(x,k) P_{\mathcal{R}}(k), \tag{76}$$

and we use the orthogonality relation of the spherical harmonics to find

$$\langle a_{\ell m} a_{\ell' m'}^* \rangle = \delta_{\ell\ell'} \delta_{mm'} \times \frac{2}{\pi} \int dk\, k^2 |\Theta_\ell(x,k)|^2 P_{\mathcal{R}}(k). \tag{77}$$

Evaluated at $x = x_0 = 0$, we find the expression for the angular CMB power spectrum today (see Eq. (69)). We can rewrite this in terms of the dimensionless primordial power spectrum $\Delta_{\mathcal{R}}^2 = k^3/(2\pi^2) P_{\mathcal{R}}(k)$. Now, the angular CMB power spectrum is given by

$$C(\ell) = 4\pi \int_0^\infty dk \frac{|\Theta_\ell(0,k)|^2}{k} \Delta_{\mathcal{R}}^2(k), \tag{78}$$

however, it is customary to present is in a scaled version $\mathcal{D}(\ell) \equiv \ell(\ell+1)(2\pi)^{-1} T_{\text{CMB0}}^2 C(\ell)$.

The cosmic variance is an unavoidable error in the estimation of $C(\ell)$, given by

$$\left(\frac{\Delta C(\ell)}{C(\ell)} \right)_{\text{cosmic variance}} = \sqrt{\frac{2}{2\ell+1}}. \tag{79}$$

Due to the fact that this is very large for small ℓ, the sums over multipole moment ℓ (in e.g. Eq. (71)) will normally start at $\ell = 2$ and stop at some ℓ_{MAX}. The monopole term ($\ell = 0$) is simply the average temperature across the CMB sky, whereas the dipole term ($\ell = 1$) is affected by our motion relative to the CMB rest frame.

We usually relate the angular wavenumber ℓ to the angular scale θ by $\theta \sim 180°/\ell$.

Source function The line-of-sight integral that gives the photon temperature multipoles $\Theta_\ell(0,k)$ can be written

$$\begin{aligned}\Theta_\ell(0,k) &= \int_{-\infty}^0 dx\, \tilde{S}(x,k) j_\ell(k[\eta_0 - \eta(x)]) \\ &\simeq \int_{\lesssim x_*}^0 dx\, \tilde{S}(x,k) j_\ell(k[\eta_0 - \eta(x)]),\end{aligned} \tag{80}$$

since (as we will see) $\tilde{S}(x,k)$ vanishes before decoupling. The temperature source function $\tilde{S}(x,k)$ can be written as the sum of four terms,

$$\tilde{S}(x,k) = (\text{SW}) + (\text{ISW}) + (\text{Doppler}) + (\text{pol}). \tag{81}$$

We will break this expression down, term by term.

The first term—the Sachs-Wolfe term—is the predominant contribution to the source function and is given by

$$(\text{SW}) = \tilde{g}(x) \left[\Theta_0(x,k) + \Psi(x,k) + \frac{1}{4} \Theta_2(x,k) \right]. \tag{82a}$$

The term originates in the gravitational redshifting of CMB photons at the surface of last scattering. For the largest scales ($\ell \lesssim 20$), the corresponding contribution to the CMB anisotropy, $C(\ell)^{\text{SW}}$, to plateau—hence the name "Sachs-Wolfe plateau". By a rough approximation, we can get to $\Theta_\ell(0,k) \approx (\Theta_0(x_*,k) + \Psi(x_*,k)) j_\ell(k\eta_0)$. Leaving the steps out, we take note that the effective temperature perturbation $[\Theta_0 + \Psi](x \leq x_*, k)$ can be used to study the basic structures of the CMB power spectrum. We do this in Sect. 5.1.2.

Also due to gravitational redshift is the integrated Sachs-Wolfe effect,

$$(\text{ISW}) = e^{-\tau(x)} \left[\frac{d\Psi(x,k)}{dx} - \frac{d\Phi(x,k)}{dx} \right]. \tag{82b}$$

It occurs between the last scatting surface and us, thus not relevant in the primordial CMB. The phenomenon arises when there is a time dependence in the gravitational potentials. Hence, in the era dominated by normal matter, this effect vanishes (there is little or no evolution to the gravitational wells and hills). We therefore speak of two sides to this effect—before and after matter domination. Following the generation of the primordial CMB, by courtesy of the (non-integrated) SW effect, the "early-time" ISW take immediate effect. As with the presence of radiation, dark energy affects the expansion of the universe and disturbs the gravitational potential. We expect to see the "late-time" ISW affecting the large-modes that entered (and enters) the horizon after matter-dark energy equality.

The Doppler effect due to our galaxy's peculiar motion relative to the CMB rest frame contributes to the source function in the form of

$$(\text{Doppler}) = -\frac{1}{ck} \frac{d}{dx} [\mathcal{H}(x) \tilde{g}(x) u_{\text{b}}(x,k)]. \tag{82c}$$

The shifted frequency and apparent deflection of the CMB photons distort $a_{\ell m}$ at all ℓs.

The smallest contribution is the quadrupole term

$$(\text{pol}) = \frac{3}{4c^2k^2} \frac{d}{dx} \left(\mathcal{H}(x) \frac{d}{dx} [\mathcal{H}(x) \tilde{g}(x) \Theta_2(x,k)] \right), \tag{82d}$$

for which we do not have a statisfying physical intuition. In any case, this term will not provide any new insights in our polarisation-free neutrino-neglecting model.

5.1.2. Effective temperature perturbation

We intend to give a high-level asymptotic analysis of the CMB power spectrum to be able to extract physics from it. For more details, see Winther et al. (2023), Dodelson & Schmidt (2021) and especially Hu (2017).

We consider the approximation on the photon multipole

$$\Theta_\ell(0,k) \approx \Theta_\ell^{\text{SW}}(0,k) \approx [\Theta_0 + \Psi](x_*,k) j_\ell(k\chi_*), \tag{83}$$

where $\chi_* = \eta_0 - \eta_* \approx \eta_0$ is the comoving distance at decoupling. The equation for this quantity describes a driven harmonic oscillator, and going back to real space and ignoring the driving force, we obtain an equation for $\delta_\gamma(t, \boldsymbol{x})$ describing waves moving at the speed of sound $c_s = c\sqrt{w_\gamma} = c/\sqrt{3}$.

Gravitational forcing   Further, it can be shown that

$$[\Theta_0 + \Psi](x,k) \approx [\Theta_0 + \Psi](x_{\mathrm{init}}, k) \cos(ks(x)) \tag{84}$$

if we keep neglecting the driving force. For fixed x, the k-modes that correspond to extrema follow a harmonic relationship $k_n = \pi/s(x)$. The crests and troughs in $\Theta_\ell(0, k)$ translate to odd and even peaks in the CMB power spectrum. A rough mapping from Fourier space to harmonic space, $k \mapsto \ell \cong k\chi_*$ (assuming no curvature), implies a coherent series of acoustic peaks in $C(\ell) \sim \cos^2(ks_*)$ at $\ell_n \approx n\ell_{\mathrm{pk}}$, where $\ell_{\mathrm{pk}} \equiv \pi\chi_*/s_*$. In the limit where $ks_* \ll 1$, the perturbation is frozen into its initial state. That is, for the largest scales in the CMB anisotropy where $\ell \ll \chi_*/s_*$, there should be no remnants of primordial acoustic oscillations.

The positions of these extrema reflects the state of the mode at recombination. With "state" is (loosely) meant whether a k-mode has succumb to gravitational pressure (maximum compression) or if the radiation pressure managed to overtake (maximum decompression), or somewhere between these extrema. We stress that the onset of such acoustic oscillations occurs after a mode has entered the horizon. The first crest in the CMB spectrum represents the mode that reached maximum compression of the primordial photon-baryon plasma just as said plasma decoupled. The subsequent peak is then the mode that compressed once inside potential wells, then rarefied before recombination. The third peak represents the mode that underwent a complete cycle of compression and decompression before being caught at its maximal compression at the surface of last scattering. The troughs of the CMB power spectrum appear at modes that are neither compressed nor decompressed at this time.

The peak locations are sensitive to the presence of curvature. We rewind a little in order to study the effect of curvature. The angular size θ of a spatial extent λ_{phys} is $\theta \approx \lambda_{\mathrm{phys}}/d_A$, where d_A is the angular diameter distance from Sect. 2.1.3. The substitution $\lambda_{\mathrm{phys}} \rightarrow {}^a\!/k$ and Eq. (17) gives $\theta \cong k^{-1}/r(\chi)$, where $r(\chi)$ is defined in Eq. (16). Now, the angular size of the sound horizon is $\varsigma(x) = s(x)/(r \circ \chi)(x)$, and evaluated at decoupling gives $\varsigma_* \equiv \varsigma(x_*) = s_*/r(\chi_*)$. This angular scale describes the typical extent of a large clump in a CMB temperature map. Now, the lowest angular wavenumber to peak in the anisotropy spectrum should be close to $\ell_{\mathrm{pk}} \equiv {}^\pi\!/\varsigma_*$, hence $\ell_{\mathrm{pk}} \propto r(\chi_*)$. Studying Eq. (16) we can see that the this lenght is smaller in a closed universe ($\Omega_{K0} < 0$) than in a flat one ($\Omega_{K0} = 0$), and the opposite for an open universe ($\Omega_{K0} > 0$), i.e. $\ell_{\mathrm{pk}}^{\mathrm{closed}} < \ell_{\mathrm{pk}}^{\mathrm{flat}} < \ell_{\mathrm{pk}}^{\mathrm{open}}$.[9] Thus, the position of the first peak (and second and third, for that matter) can be used to constrain the curvature density Ω_{K0}. Since the Euclidian analysis predicts $\ell_{\mathrm{pk}}^{\mathrm{flat}} = \pi\chi_*/s_*$, if the actual (observed) peak is shifted e.g. towards higher multipoles (usually to the left), one could argue that the universe must be hyperbolic. However, one need keep in mind the parameter degeneracy and the ambiguity of our mapping from Fourier space to spherical harmonic space.

Baryon loading   We consider the effect of baryon loading. The slightly less simplified analysis gives

$$[\Theta_0 + (1+R)\Psi](x,k) \approx [\Theta_0 + (1+R)\Psi](x_{\mathrm{init}}, k) \cos(ks(x)) \tag{85}$$

where $R(x) = {}^3\!/4\,\Omega_{\mathrm{b}0}\mathrm{e}^x/\Omega_{\gamma 0}$ as before. The offsat oscillations in the effective tempeature $[\Theta_0 + \Psi](x, k)$ are visible in $C(\ell)$

---

[9] One arrives at the same conclusion from a geometrical analysis of the perturbation scales (angular size) in the three different realisations of the background geometry.

---

as variations in the amplitudes of the peaks. The presence of baryons has the effect that odd peaks are enhanced, whilst even peaks are suppressed.

The physical understanding is that more baryons loads down the plasma in a potential well, giving rise to asymmetric oscillations. For the effect to take place, the amount of baryons in the universe has to be such that their gravitational pull is non-negligable compared to that of the dark matter. In other words, the effect of baryon loading is strongly scaled with the relative composition of normal matter in the universe (e.g. $\Omega_{\mathrm{b}0}/\Omega_{\mathrm{m}0}$).

Radiation driving   Radiation drives acoustic oscillations by introducing temporal variations in the gravitational potential. The always-decreasing background density will cause potentials to decay *unless* there are unimpeded growth in the density perturbations in the dominant energy component. For a mode entering the horizon in the radiation dominated era, the radiation pressure begins fighting gravity at the first point of maximal fluid compression, and the gravitational potentials necessarily must decay. The subsequent phase of rarification does not include this fight and the amplitude is driven up. Thus, sub-horizon modes in the radiation dominated universe will be enhanced. This relates the power of the (average) CMB power spectrum at these scales ($\ell \gtrsim 100$) to the ratio of dark matter and radiation in the universe. In eliminating gravitational potentials, acoustic oscillations in the photon-baryon plasma eliminate the heights in the alternating peaks from baryon loading. Note that it is separable from the baryonic effects with the first three peaks or more.

Diffusion damping   Recombination did not occur instantaneously, and as such, the photons bounce around the baryons during the short period it takes for the universe to recombine. Consider a photon in a sea of electrons. Should a random walk take said photon from one region of temperature perturbation scale to another, the photon will try to blend in with other photons, resulting in a mixed temperatures at the scales in question. For fluctuations with wavelength smaller than the mean comoving distance a photon travels of order

$$\lambda_D \sim \lambda_{\mathrm{mfp}} \sqrt{n_e \sigma_{\mathrm{T}} H^{-1}} = \frac{1}{\sqrt{n_e(x)\sigma_{\mathrm{T}}\mathcal{H}(x)\mathrm{e}^x}}, \tag{86}$$

hot and cold photons will mix. As a result, the temperature perturbations are washed out for $k \gtrsim k_D = 2\pi/\lambda_D$. We expect to see this as a *damping tail* in the CMB power spectrum at particularly small scales.

5.1.3. Matter power spectrum

The dimensionless function

$$\Delta_s(x,k) = \delta_s(x,k) - \frac{3(1+w_s)\mathcal{H}(x)}{ck} u_s(x,k) \tag{87}$$

is a gauge-invariant density perturbation used to measure the linear power spectrum of species s at time x and comoving wavenumber k. For the total (linear) matter power spectrum $P_{\mathrm{m}}(x,k)$, we use

$$\delta_{\mathrm{m}}(x,k) = \frac{\delta_{\mathrm{c}}(x,k)\Omega_{\mathrm{c}}(x) + \delta_{\mathrm{b}}(x,k)\Omega_{\mathrm{b}}(x)}{\Omega_{\mathrm{m}}(x)}$$

$$u_{\mathrm{m}}(x,k) = \frac{u_{\mathrm{c}}(x,k)\Omega_{\mathrm{c}}(x) + u_{\mathrm{b}}(x,k)\Omega_{\mathrm{b}}(x)}{\Omega_{\mathrm{m}}(x)} \tag{88}$$

in Eq. (87) to find

$$P_{\mathrm{m}}(x, k) = |\Delta_{\mathrm{m}}(x, k)|^2 P_{\mathcal{R}}(k). \tag{89}$$

We focus on this spectrum today, $P_{\mathrm{m0}}(k) \equiv P_{\mathrm{m}}(x = 0, k)$. In short, this function is broad and has a turnover at $k \simeq k_{\mathrm{eq}}$, i.e. $\max P_{\mathrm{m0}}(k) \simeq P_{\mathrm{m0}}(k_{\mathrm{eq}})$. As density perturbations hardly grow inside the horizon in the radiation-dominated era, the small-scale power spectrum is suppressed relative to its large-scale counterpart. The largest scale for which we get suppression is represented by the k-mode that enters the horizon at matter-radiation equality—hence the peak at the equality scale.

Dodelson & Schmidt (2021) shows that at late times, the approximation

$$\Delta_{\mathrm{m}}(x, k) = \frac{c^2 k^2 \mathrm{e}^x}{\sfrac{3}{2}\Omega_{\mathrm{m0}}H_0^2} \Phi(x, k); \quad x \gtrsim x_\Lambda, \quad k \gg \mathcal{H}(x), \tag{90}$$

suffices when neglecting massive neutrinos. Thus, for the power spectrum today, we expect $P_{\mathrm{m0}}(k \ll k_{\mathrm{eq}}) \propto k^4 P_{\mathcal{R}}(k) \propto k^{n_{\mathrm{s}}}$.

We consider a single perturbation (a peak) of normal and matter and relativistic matter in real space at early times. Once photons decoupled from baryons and travelled freely, a spherical shell of baryonic matter surrounding our peak is dragged somewhat out from the sound horizon at decoupling before it falls into potential wells with the CDM. As time goes by, CDM starts to cluster around this shell. The linearity of the perturbations lets us imagine many such peaks with equally large shells of matter surrounding them. In Fourier space, this corresponds to oscillatory behaviour in k of scale $\sim s_*$. Thus, we expect to see small oscillations in the small-scale part of the total matter power spectrum.

5.2. Implementation details

We wrote a C++ code that uses the class objects from the previous sections and three additional parameters; primordial amplitude $\mathcal{A}_{\mathrm{s}}$, spectral index n_{s} and pivot scale k_{p}. We used the following fiducial values:

$$\mathcal{A}_{\mathrm{s}} = 2.1 \times 10^{-9}$$
$$n_{\mathrm{s}} = 0.965$$
$$k_{\mathrm{p}} = 0.05 \, \mathrm{Mpc}^{-1} \tag{91}$$

There were three main computations to this problem: the work of finding $j_\ell(z)$, where $z = k(\eta_0 - \eta(x))$, and $\Theta_\ell(0, k)$ for a set of ℓs, then computing (and interpolating) $C(\ell)$. We do not solve any differential equations, but rather use the very powerful trapezoidal rule to evaluate our integrals. For a fixed step size Δz, this rule takes the simple form

$$\int_{z_0}^{z_N} \mathrm{d}z \, f(z) \approx \Delta z \left(\sum_{j=1}^{N-1} f(z_j) + \frac{f(z_0) + f(z_N)}{2} \right); \quad N = \frac{z_N - z_0}{\Delta z}. \tag{92}$$

In preparation of the necessary computations, we chose a set of ℓs, call it L, for which to perform the line-of-sight integration. We let $L \subset \mathcal{L} \equiv \{2, 3, \ldots, \ell_{\mathrm{MAX}}\}$ be a clever choice of a number of integers[10] $\ell \in \mathcal{L}$. The resolution in the subdomain L needs to be such that oscillatory information is not lost in going from $C(\ell \in L) \to C(\ell \in \mathcal{L})$. We let $\ell_{\mathrm{MAX}} = 2000 \in L$ be the highest multipole we consider.

---

[10] $\#L = 63$, to be exact.

(1) To generate the spherical Bessel functions, we utilised the functionalities of GSL. We loop through $\ell \in L$ and, for each iteration, collected the $j_\ell(z)$'s from GSL for $z = 0, \Delta z, 2\Delta z, \ldots, k_{\mathrm{max}}\eta_0$, where $\Delta z = 2\pi/n_{\mathrm{samp}}$. To properly sample the oscillations, we used $n_{\mathrm{samp}} = 20$.

(2) For the computation of $\Theta_\ell(0, k)$, we designed a grid of ℓ-, k- and x-values. Naturally, we considered $\ell \in L$. The resolution for $k \in [k_{\mathrm{min}}, k_{\mathrm{max}}]$ will be addressed shortly. The integration in Eq. (80) was started from $x = -8.3$ with step size $\Delta x = 2\pi/n_{\mathrm{samp}}$ in Eq. (92). This time we used $n_{\mathrm{samp}} = 500$.

(3) We solved Eq. (78) for $C(\ell \in L)$ using the trapezoidal rule in Eq. (92) with $z \to \ln k$. That is, we solved

$$C(\ell) = 4\pi \int_{\ln k_{\mathrm{min}}}^{\ln k_{\mathrm{max}}} \mathrm{d}\ln k \, |\Theta_\ell(0, k)|^2 \Delta_{\mathcal{R}}^2(k) \tag{93}$$

with a fixed step size $\Delta \ln k$, determined by the sampling

$$\eta_0 \Delta k \overset{!}{=} \frac{2\pi}{n_{\mathrm{samp}}} \rightsquigarrow N_k = \frac{k_{\mathrm{max}} - k_{\mathrm{min}}}{\Delta k} \overset{!}{=} N_{\ln k} = \frac{\ln k_{\mathrm{max}} - \ln k_{\mathrm{min}}}{\Delta \ln k}. \tag{94}$$

In this case, we used $n_{\mathrm{samp}} = 32$. We interpolated over L to find $C(\ell \in \mathcal{L})$.

5.2.1. Parallelisation

A large part of these computations are independent and could therefore be executed in parallel. We applied OpenMP parallelisation to all three jobs, improving their individual performances significantly. The details will not be discussed in this paper.

5.3. Results

As functions of wavenumber k, we plot the transfer function for a set of angular wavenumbers $\ell \in \{6, 100, 200, 500, 1000\}$ in Fig. 12. For the a smaller range of values of k, we also plot the interesting part of the integrand in the expression for the CMB power spectrum.

The CMB power spectrum is presented in Fig. 13. Note that we used the scaled quantity $\mathcal{D}(\ell)$. The different contributions to the CMB anisotropy were overplotted, as well as the cosmic variance from Eq. (79). We included observational data from Planck Collaboration et al. (2021) for low ℓ. Observational data become less relevant for $\ell \gtrsim 200$ as effects of e.g. neutrinos are non-negligible at these scales. The contributions to the CMB spectrum were calculated as follows, where $[\mathrm{comp}] \in \{\mathrm{SW}, \mathrm{ISW}, \mathrm{Doppler}, \mathrm{pol}\}$ are the terms in the source function ($\tilde{S}(x, k) \supset ([\mathrm{comp}])$, see Eq. (81)) given by Eq. (82):

$$\mathcal{D}(\ell)^{[\mathrm{comp}]} = \frac{\ell(\ell+1)T_{\mathrm{CMB0}}^2}{2\pi} C(\ell)^{[\mathrm{comp}]};$$

$$C(\ell)^{[\mathrm{comp}]} = 4\pi \int_0^\infty \mathrm{d}k \, \frac{\left|\Theta_\ell^{[\mathrm{comp}]}(0, k)\right|^2}{k} \Delta_{\mathcal{R}}^2(k);$$

$$\Theta_\ell^{[\mathrm{comp}]}(0, k) = \int_{-\infty}^0 \mathrm{d}x \, ([\mathrm{comp}]) j_\ell(k[\eta_0 - \eta(x)]) \tag{95}$$

We found the fundametal tone at $\ell_1 = 205$. The next two peaks werw located at $\ell_2 = 490$ and $\ell_3 = 727$. Higher peaks were found at $\ell_4 = 1008$, $\ell_5 = 1273$, $\ell_6 = 1552$ and $\ell_7 = 1825$.
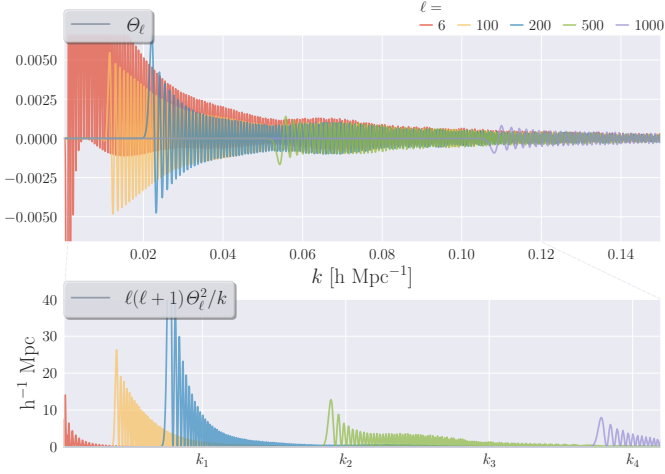
Fig. 12: The photon transfer functions $\Theta_\ell(0, k)$ as functions of wavenumber k for a set of angular wavenumbers ℓ. We extracted a part of the x-axis for which to show $\ell(\ell + 1) \times \frac{1}{k}|\Theta_\ell(0,k)|^2$ as functions of k, now with emphasis on the fundamental scale for which $k_n = nk_1$.
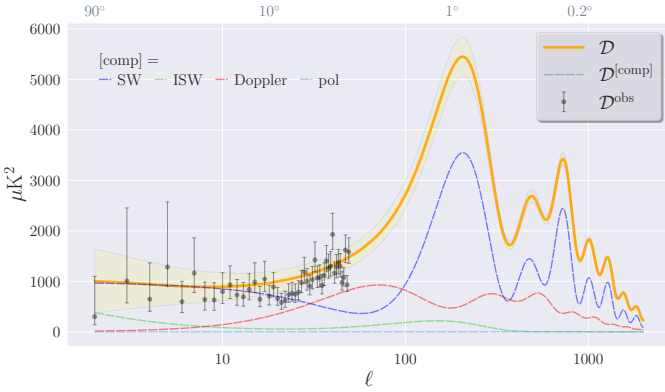
Fig. 13: The scaled CMB power spectrum $\mathcal{D}(\ell)$ as function of multipole moment ℓ. The shaded region represents the fundamental cosmic variance. Upper axis demonstrates corresponding angular scale $\sim 180°/\ell$. Observational data are included for large scales.

In figure Fig. 14 is plotted the total matter power spectrum. Observational data from Hlozek et al. (2012) and Planck Collaboration et al. (2021) is shown in the same figure. Discrepancy is significantly larger for smaller scales.
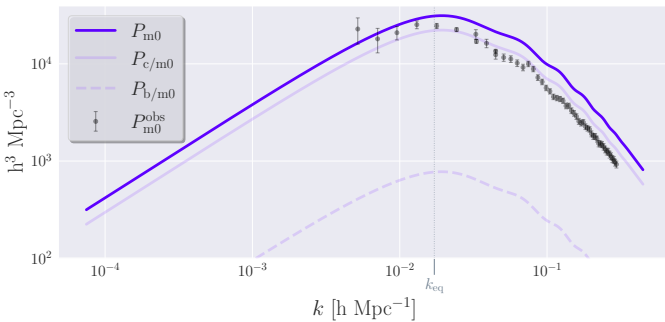
Fig. 14: The total matter power spectrum (today) $P_{m0}(k)$ as function of wavenumber k. Both axes are logarithmic. The equality scale k_{eq} is demonstrated by a vertical dotted line. The individual contributions from CDM and baryons and observational data are included.

5.4. Discussion

The transfer functions in Fig. 12 describe how the primordial density fluctuations at a particular angular wavenumber ℓ depend on comoving wavenumber k. The LOS integration encapsulates complex physics introduced by the source function. For starters, it provides an image of the relationship between k and ℓ which is not one-to-one. For example, $\ell = 200$ encapsulates physics at wavenumbers 0.02 Mpc$^{-1} \lesssim k/h \lesssim 0.05$ Mpc^{-1}.

The multipole numbers considered in Fig. 12 deserve some attention. Note that Fig. 13 is complementary to this discussion. $\ell = 6$ probes large-scale physics where $C(\ell) \propto \ell(\ell + 1)$, and by extension, the initial conditions. It is asymmetric around the k-axis, as opposed to the higher multipoles we see in the upper panel of Fig. 12. This "lift" is due to the late ISW effect (c.f. Fig. 11 at $x > x_\Lambda$); without DE domination the prediction is $\Theta_{\ell \lesssim 30}(0, k) \propto j_\ell(k\eta_0)$, which is asymptotically symmetric. $\ell = 100$ translates to k-modes that entered the horizon in or around the period between matter-radiation equality and recombination. These scales did not manage a complete compression in the primordial plasma before decoupling, but rather were caught in states of increasing photon overdensities, i.e. compressing in potential wells resulting in higher photon temperature.

We see that the higher multipoles correspond roughly to angular peaks in the CMB power spectrum, in particular the first $\ell_1 \approx 200$, the second $\ell_2 \approx 500$ and the fourth $\ell_4 \approx 1000$. The first represents a compression, evident from the direction of the onset of oscillations in the transfer function, or simply from its encapsulation of the k_1-mode. The second and fourth peak are decompressions, which we can see from similar arguments.

5.4.1. CMB anisotropy

We turn to the main result of this project in Fig. 13. The Sachs-Wolfe and Doppler contributions to the CMB anisotropy are by far most significant in order to reproduce the observed spectrum. We notice the Sachs-Wolfe plateau for small ℓ. The polarisation term is negligible in our model.

The power at the SW plateau is sensitive to the primordial amplitude and substantiate the fiducial value $\mathcal{A}_s \sim 10^{-9}$. The tilt in the purely SW contribution ($\mathcal{D}(\ell)^{SW} > \mathcal{D}(\ell')^{SW} \, \forall \, \ell < \ell' \lesssim 30$) is there because the scalar spectral index is less than 1. That is, $n_s \approx 0.96$ in the primordial power spectrum is also a result of a fitting analysis at these scales—corresponding to angular separations on the sky of $\sim 90°$—in the CMB anisotropy.

The late- and early-time ISW effects show themselves as enhancements in the CMB power spectrum at scales $\lesssim 10°$ and $\sim 1°$, respectively. The photons we observe have propagated through large-scale superclusters (voids) of shrinking depths (heights), hoisting (depriving) propagating photons of their entitled energy as they exit the potential wells (hills).

Angular peaks As we know, modes caught in states of extrema at the time of recombination make up the angular peaks—the peaks in the CMB power spectrum. We see that the mode that compressed once inside potential wells prior to recombination corresponds to angular wavenumber $\ell \sim 200$, that is an angular size of $\sim 1°$. The second peak is significantly suppressed relative to the first and third peak. As the odd peaks represent compressions in the photon-baryon plasma, this result gives a clear indication of a preeminent contribution from CDM to the total matter.

The damping tail—the suppression in Fig. 13 for $\ell \gtrsim 800$—is the result of diffusion damping for small scales discussed in Sect. 5.1.2.

5.4.2. Matter inhomogeneity

Oscillations in the matter power spectrum in Fig. 14 are only present for the small-scale modes ($k > k_{eq}$), as we expected. These acoustic wiggles in Fourier space reflect the shell-like clustering of matter in real space at sound horizon radii.

During radiation domination, the CDM overdensities on sub-horizon scales grow very fast. Thus, for modes $k > k_{eq}$, the dimensionless power spectrum simply grows with increasing k as this corresponds to increasingly accumulating CDM overdensity. Accounting for the primordial power spectrum $P_{\mathcal{R}}(k) \propto k^{n_s-4}$, the effects on the small-scale modes are supressed. Despite the relative enhancement of effects on large-scale modes from the primordial spectrum, the matter power spectrum is suppressed for decreasing k at modes $k < k_{eq}$.

The position of the peak is sensitive to the matter-radiation equality and is thus a probe of the energy density ratio between radiation and matter in the universe, Ω_{r0}/Ω_{m0}.

The graph's poor coherence with observational data for intermediate- and small-scale modes is most likely a concequence of the simplicity of our model. We note that $\Omega_{r0}/\Omega_{m0} \mathrel{\widehat{=}} \Omega_{\gamma0}/\Omega_{m0}$ in our case, and therefore expect this to be a little shifted *to the left* when including neutrinos in the background.

6. Conclusion

We used fiducial parameters in the ΛCDM concordance model of cosmology to calcuate the CMB anisotropy spectrum. The preparations from Sects. 2 & 3 lead to vanilla results in Sects. 4 & 5 that were satisfactory, more so on large scales. We did not expect the final results to be perfectly coherent with observational data, but rather use them to understand the physical mechanisms we considered in out model.

We acknowledge the inconsistency from the ambigous N_{eff}-value in this paper. In refusing to perturb neutrino-related quantities, one also fiddles with the neutrino-keeping background in an unfortunate way, so they should be ignored completely.

Further improvements include rewriting parts of the code to account for secondary physical mechanisms. Particularly we would add helium and followingly reionisation in Sect. 3 and account for neutrino perturbations and photon polarisation in Sect. 4. To get more hands-on experience with the physical implications of the CMB anisotropy, one should experiment with parameters systematically.

References

Baumann, D. 2015, Cosmology: Part III Mathematical Tripos

Betoule, M., Kessler, R., Guy, J., et al. 2014, A&A, 568, A22

Callin, P. 2006, arXiv e-prints, astro

Dodelson, S. & Schmidt, F. 2021, Modern Cosmology, 2nd edn.

Hlozek, R., Dunkley, J., Addison, G., et al. 2012, The Astrophysical Journal, 749, 90

Hu, W. 2017, waynehu, accessed online May 21st 2023 at `http://background.uchicago.edu/~whu/index.html`

Ma, C.-P. & Bertschinger, E. 1995, ApJ, 455, 7

Peebles, P. J. E. 1968, ApJ, 153, 1

Planck Collaboration, Aghanim, N., Akrami, Y., et al. 2021, A&A, 652, C4

Winther, H. A., Eriksen, Hans K., E., Øystein, Mota, D. F., & Ihle, H. 2023, Cosmology II, accessed online May 21st 2023 at `https://cmb.wintherscoming.no/index.php`

Appendix A: Conformal Hubble parameter

Revisit the general form of the first Friedmann equation from Sect. 2.1.2, i.e.

$$\mathcal{H}(x) = H_0 \sqrt{\sum_s \Omega_{s0} e^{-(1+3w_s)x}}, \tag{A.1}$$

where sum over s is a sum over the constituents in the universe ($s \in \{m, r, \Lambda, K\}$) and w_s represents the species' equation of state parameter. As a shorthand notation, we introduce $\Xi_m = \Xi_m(x)$ given by

$$\Xi_m(x) \equiv \sum_s (-1)^m (1 + 3w_s)^m \Omega_{s0} e^{-(1+3w_s)x}; \quad m \in \mathbb{N}, \tag{A.2}$$

s.t. $\mathrm{d}^n X_m/\mathrm{d}x^n = \Xi_{m+n}$. Now $\mathcal{H} = H_0 \sqrt{\Xi_0}$ and its first derivative becomes

$$\frac{\mathrm{d}\mathcal{H}}{\mathrm{d}x} = H_0 \frac{\Xi_1}{2\sqrt{\Xi_0}}. \tag{A.3}$$

The second derivative is obtained through the quotient rule, i.e.

$$\frac{\mathrm{d}^2\mathcal{H}}{\mathrm{d}x^2} = \frac{H_0}{2} \frac{\Xi_2 \sqrt{\Xi_0} - \Xi_1 \frac{\Xi_1}{2\sqrt{\Xi_0}}}{\Xi_0}$$
$$= H_0 \frac{\Xi_1}{2\sqrt{\Xi_0}} \left(\frac{\Xi_2}{\Xi_1} - \frac{\Xi_1}{2\Xi_0} \right). \tag{A.4}$$

Now that we have these expressions, let us look at some special cases. Assume that the universe only consists of the substance s. Then

$$\Xi_m = (-1)^m (1 + 3w_s)^m \Omega_{s0} e^{-(1+3w_s)x}. \tag{A.5}$$

We obtain the following:

$$\frac{1}{\mathcal{H}} \frac{\mathrm{d}\mathcal{H}}{\mathrm{d}x} = \frac{\Xi_1}{2\Xi_0} \qquad = -\frac{1}{2}(1 + 3w_s) \tag{A.6a}$$

$$\frac{1}{\mathcal{H}} \frac{\mathrm{d}^2\mathcal{H}}{\mathrm{d}x^2} = \frac{\Xi_1}{2\Xi_0}\left(\frac{\Xi_2}{\Xi_1} - \frac{\Xi_1}{2\Xi_0}\right) = +\frac{3}{4}(1 + 3w_s)^2 \tag{A.6b}$$

As for the conformal time, we get an expression that is ill-defined for some cases:

$$\frac{\eta\mathcal{H}}{c} = \mathcal{H} \int_{-\infty}^{x} \mathrm{d}x' \frac{1}{\mathcal{H}}$$
$$= e^{\frac{x}{2}(1+3w_s)} \int_{-\infty}^{x} \mathrm{d}x' \, e^{-\frac{x'}{2}(1+3w_s)}$$
$$= \begin{cases} \frac{2}{1+3w_s} & w_s > 1/3 \\ \infty & w_s \leq -1/3 \end{cases} \tag{A.7}$$

We have gathered a set of analytical predictions for different eras in the history of the universe. The detailed result is presented in Table A.1. Note, however, that to compare this last expression to the numerical result does not actually make sense for later times as $\eta(x)$ depends on the historic composition as well.

Appendix B: Perturbation equations

This appendix contains equations relevant for Sect. 4.

We let $' \equiv \frac{\mathrm{d}}{\mathrm{d}x}$ in the equations below. Additionally, we introduce $\mathcal{Y} = \mathcal{Y}(x, k) \equiv \frac{ck}{\mathcal{H}(x)}$ as a shorthand notation.

Table A.1: Analytical predictions for single-substance universes.

	w_s	$\mathcal{H}/H_0$	$\frac{1}{\mathcal{H}}\frac{\mathrm{d}\mathcal{H}}{\mathrm{d}x}$	$\frac{1}{\mathcal{H}}\frac{\mathrm{d}^2\mathcal{H}}{\mathrm{d}x^2}$	$\frac{\eta\mathcal{H}}{c}$
Radiation-dominated	$1/3$	$\sqrt{\Omega_{r0}}e^{-x}$	-1	1	1
Matter-dominated	0	$\sqrt{\Omega_{m0}}e^{-1/2 x}$	$-1/2$	$1/4$	2
DE-dominated	-1	$\sqrt{\Omega_{\Lambda 0}}e^{x}$	1	1	∞

Appendix B.1: The full system

The metric perturbations evolve as follows:

$$\Phi' = \Psi - \frac{\mathcal{Y}^2}{3}\Phi + \frac{H_0^2}{2\mathcal{H}^2 e^{2x}}\left\{(\Omega_{c0}\delta_c + \Omega_{b0}\delta_b)e^x + 4\Omega_{\gamma 0}\Theta_0\right\} \tag{B.1a}$$

$$\Psi = -\Phi - \frac{12H_0^2}{c^2 k^2 e^{2x}}\Omega_{\gamma 0}\Theta_2 \tag{B.1b}$$

Note that Eq. (B.1b) is not a differential equation. The perturbations to normal matter ($s = c, b$) are the following:

$$\delta_s' = \mathcal{Y}u_s - 3\Phi' \tag{B.2a}$$

$$u_s' = -u_s - \mathcal{Y}\Psi + \delta_{sb}\frac{\tau'}{R}(3\Theta_1 + u_b) \tag{B.2b}$$

The monopole and dipole evolves as:

$$\Theta_0' = -\mathcal{Y}\Theta_1 - \Phi' \tag{B.3a}$$

$$\Theta_1' = \frac{\mathcal{Y}}{3}[\Theta_0 - 2\Theta_2 + \Psi] + \tau'\left[\Theta_1 + \frac{u_b}{3}\right] \tag{B.3b}$$

For the quadrupole and higher multipoles, we have:

$$\Theta_\ell' = \begin{cases} \frac{\mathcal{Y}}{2\ell+1}[\ell\Theta_{\ell-1} - (\ell+1)\Theta_{\ell+1}] + \frac{9}{10}\tau'\Theta_\ell & \ell = 2 \\ \frac{\mathcal{Y}}{2\ell+1}[\ell\Theta_{\ell-1} - (\ell+1)\Theta_{\ell+1}] + \tau'\Theta_\ell & 2 < \ell < \ell_{max} \\ \mathcal{Y}\Theta_{\ell-1} - \frac{c(\ell+1)}{\mathcal{H}\eta}\Theta_\ell + \tau'\Theta_\ell & \ell = \ell_{max} \end{cases} \tag{B.3c}$$

Appendix B.2: Tight coupling regime

The tight coupling regime considers Eq. (B.1), Eq. (B.3a) and Eq. (B.2) except for Eq. (B.2b) for $s = b$. The following equations substitute the missing derivatives Θ_1' and u_b':

$$u_b' = \frac{q - Ru_b + \mathcal{Y}(-\Theta_0 + 2\Theta_2)}{1+R} - \mathcal{Y}\Psi \tag{B.4a}$$

$$\Theta_1' = \frac{1}{3}\left(q - u_b'\right) \tag{B.4b}$$

q is given by:

$$q = \left[\tau'(1+R) - R\left(1 - \frac{\mathcal{H}'}{\mathcal{H}}\right)\right]^{-1} \times$$
$$\left\{ -[\tau''(1+R) - \tau'(1-R)](3\Theta_1 + u_b) \right.$$
$$\left. - \mathcal{Y}R\left[\Psi - \left(1 - \frac{\mathcal{H}'}{\mathcal{H}}\right)(-\Theta_0 + 2\Theta_2) + \Theta_1'\right]\right\} \tag{B.4c}$$

The higher multipoles are given by Eq. (B.7)

Appendix B.3: Initial conditions

Let $\Psi_{\text{init}} \equiv \Psi(x_{\text{init}}, k)$ and $k\eta(x_{\text{init}}) \ll 1$. Further, we use that $\Psi_{\text{init}} = -{}^2\!/_3$ and the following scalar quantities at $x = x_{\text{init}}$:

$$\Phi(x_{\text{init}}, k) = -\Psi_{\text{init}} \tag{B.5a}$$

$$\delta_s(x_{\text{init}}, k) = -\frac{3}{2}\Psi_{\text{init}} \,; \qquad\qquad s = \text{c, b} \tag{B.5b}$$

$$u_s(x_{\text{init}}, k) = -\frac{\mathcal{Y}(x_{\text{init}}, k)}{2}\Psi_{\text{init}} \,; \qquad s = \text{c, b} \tag{B.5c}$$

The first two photon multipoles are given by the following:

$$\Theta_0(x_{\text{init}}, k) = -\frac{1}{2}\Psi_{\text{init}} \tag{B.6a}$$

$$\Theta_1(x_{\text{init}}, k) = +\frac{\mathcal{Y}(x_{\text{init}}, k)}{6}\Psi_{\text{init}} \tag{B.6b}$$

For the quadrupole and the remaining multipoles, the following expressions hold at early times:

$$\Theta_2(x, k) = -\frac{4\mathcal{Y}(x, k)}{9\tau'(x)}\Theta_1(x, k) \tag{B.7a}$$

$$\Theta_\ell(x, k) = -\frac{\ell}{2\ell + 1}\frac{\mathcal{Y}(x, k)}{\tau'(x)}\Theta_{\ell-1}(x, k)\,; \quad \ell > 2 \tag{B.7b}$$

Appendix C: Temperature source function

The purpose of this appendix is to give the full equation for the photon temperature source function $\tilde{S} = \tilde{S}(x, k)$ as defined in Eq. (60).

We begin with the expression from Callin (2006, Eq. (40)):

$$\tilde{S} = \tilde{g}\left[\Theta_0 + \Psi + \frac{\Theta_2}{4}\right] + e^{-\tau}\left[\frac{\mathrm{d}\Psi}{\mathrm{d}x} - \frac{\mathrm{d}\Phi}{\mathrm{d}x}\right]$$
$$- \frac{1}{ck}\underbrace{\frac{\mathrm{d}}{\mathrm{d}x}(\mathcal{H}\tilde{g}u_{\mathrm{b}})}_{\mathfrak{U}_1} + \frac{3}{4c^2k^2}\underbrace{\frac{\mathrm{d}}{\mathrm{d}x}\left[\mathcal{H}\frac{\mathrm{d}}{\mathrm{d}x}(\mathcal{H}\tilde{g}\Theta_2)\right]}_{\mathfrak{U}_2} \tag{C.1}$$

The goal is to rewrite $\mathfrak{U}_1$ and $\mathfrak{U}_2$ in terms of quantities that we have already got. We assume that the perturbed system is already solved. The job is essentially to use the Leibniz over and over again. We make use of the shorthand $' \equiv \frac{\mathrm{d}}{\mathrm{d}x}$ from before. For $f = u_{\mathrm{b}}, \Theta_2$, the following will prove useful:

$$(\mathcal{H}\tilde{g}f)' = \mathcal{H}'\tilde{g}f + \mathcal{H}(\tilde{g}'f + \tilde{g}f') \tag{C.2a}$$

$$(\mathcal{H}\tilde{g}f)'' = \mathcal{H}''\tilde{g}f + 2\mathcal{H}'(\tilde{g}'f + \tilde{g}f') + \mathcal{H}(\tilde{g}''f + 2\tilde{g}'f' + \tilde{g}f'') \tag{C.2b}$$

We have got that

$$[\mathcal{H}(\mathcal{H}\tilde{g}\Theta_2)']' = \mathcal{H}'(\mathcal{H}\tilde{g}\Theta_2)' + \mathcal{H}(\mathcal{H}\tilde{g}\Theta_2)'', \tag{C.3}$$

so:

$$\mathfrak{U}_1 = \mathcal{H}'\tilde{g}u_{\mathrm{b}} + \mathcal{H}\left(\tilde{g}'u_{\mathrm{b}} + \tilde{g}u_{\mathrm{b}}'\right) \tag{C.4a}$$

$$\mathfrak{U}_2 = 3\mathcal{H}\mathcal{H}'(\tilde{g}'\Theta_2 + \tilde{g}\Theta_2') + \mathcal{H}^2(\tilde{g}''\Theta_2 + 2\tilde{g}'\Theta_2' + \tilde{g}\Theta_2'')$$
$$+ \left[(\mathcal{H}')^2 + \mathcal{H}\mathcal{H}''\right]\tilde{g}\Theta_2 \tag{C.4b}$$

In inserting Eq. (C.4) into Eq. (C.1), we can compute the temperature source function from our quantities and their derivatives. However, we want to avoid too many numerical vulnerabilities

and will therefore provide the expression for Θ_2'' as well. We differentiate Eq. (B.3c) with $\ell = 2$ and get

$$\Theta_2'' = \frac{1}{5}\left(\mathcal{Y}'[2\Theta_1 - 3\Theta_3] + \mathcal{Y}\left[2\Theta_1' - 3\Theta_3'\right]\right) + \frac{9}{10}(\tau''\Theta_2 + \tau'\Theta_2')$$

$$= \frac{\mathcal{Y}}{5}\left(-\frac{\mathcal{H}'}{\mathcal{H}}[2\Theta_1 - 3\Theta_3] + \left[2\Theta_1' - 3\Theta_3'\right]\right) + \frac{9}{10}(\tau''\Theta_2 + \tau'\Theta_2')$$

$$= \frac{2\mathcal{Y}}{5}\left(\Theta_1' - \frac{\mathcal{H}'}{\mathcal{H}}\Theta_1\right) - \frac{3\mathcal{Y}}{5}\left(\Theta_3' - \frac{\mathcal{H}'}{\mathcal{H}}\Theta_3\right) + \frac{9}{10}(\tau''\Theta_2 + \tau'\Theta_2'), \tag{C.5}$$

where in the second line we used that $\mathcal{Y}' = (ck/\mathcal{H})' = -\mathcal{Y}\mathcal{H}'/\mathcal{H}$. Finally, by inserting Eq. (C.5) in Eq. (C.4b), we are ready to compute $\tilde{S}(x, k)$ in a numerically stable fashion.